ACS PHYSICAL CHEMISTRY Au
AN OPEN ACCESS JOURNAL OF THE AMERICAN CHEMICAL SOCIETY

pubs.acs.org/physchemau
Article

Rational Design of Far-Red Archaerhodopsin-3-Based Fluorescent Genetically Encoded Voltage Indicators: from Elucidation of the Fluorescence Mechanism in Archers to Novel Red-Shifted Variants

Dmitrii M. Nikolaev, Vladimir N. Mironov, Ekaterina M. Metelkina, Andrey A. Shtyrov, Andrey S. Mereshchenko, Nikita A. Demidov, Sergey Yu. Vyazmin, Tatiana B. Tennikova, Svetlana E. Moskalenko, Stanislav A. Bondarev, Galina A. Zhouravleva, Andrey V. Vasin, Maxim S. Panov, and Mikhail N. Ryazantsev*

Cite This: *ACS Phys. Chem Au* 2024, 4, 347−362

Read Online

ACCESS | Metrics & More | Article Recommendations | Supporting Information

ABSTRACT: Genetically encoded voltage indicators (GEVIs) have found wide applications as molecular tools for visualization of changes in cell membrane potential. Among others, several classes of archaerhodopsin-3-based GEVIs have been developed and have proved themselves promising in various molecular imaging studies. To expand the application range for this type of GEVIs, new variants with absorption band maxima shifted toward the first biological window and enhanced fluorescence signal are required. Here, we integrate computational and experimental strategies to reveal structural factors that distinguish far-red bright archaerhodopsin-3-based GEVIs, Archers, obtained by directed evolution in a previous study (McIsaac et al., *PNAS,* 2014) and the wild-type archaerhodopsin-3 with an extremely dim fluorescence signal, aiming to use the obtained information in subsequent rational design. We found that the fluorescence can be enhanced by stabilization of a certain conformation of the protein, which, in turn, can be achieved by tuning the pK_a value of two titratable residues. These findings were supported further by introducing mutations into wild-type archeorhodopsin-3 and detecting the enhancement of the fluorescence signal. Finally, we came up with a rational design and proposed previously unknown Archers variants with red-shifted absorption bands (λ_{max} up to 640 nm) and potential-dependent bright fluorescence (quantum yield up to 0.97%).

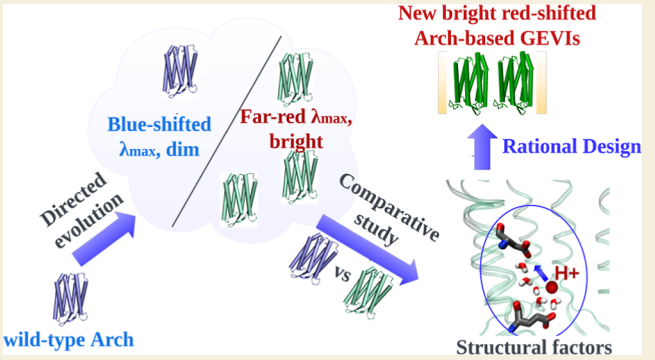

KEYWORDS: *rhodopsins, fluorescent rhodopsins, optogenetics, genetically encoded voltage indicators, GEVI, protein design*

1. INTRODUCTION

Archaerhodopsin-3-based genetically encoded voltage indicators (GEVIs) have recently found various applications in cell voltage imaging.[1−5] A number of advantageous properties of the wild-type archaerhodopsin-3 from *Halorubrum sodomense* (Arch), such as high expression level in eukaryotic cells,[6] submillisecond response time,[7] and high voltage sensitivity of fluorescence signal,[7] make this protein a promising candidate as an effective GEVI. However, an extremely low fluorescence quantum yield of the wild-type Arch (0.01%[7]), non-negligible proton-pumping photocurrent, and the lack of significant absorption in the biological optical window (650−900 nm[7]) drastically limit its applications. Several research groups applied directed evolution approaches to optimize Arch properties and developed new bright variants. Three classes of Arch-based GEVIs (QuasArs,[8] Archers,[9,10] and Archons[11]) have been proposed. Table 1 provides related properties for the most widely used representatives from each class. Comparing with the wild-type Arch, all engineered variants exhibit a considerable increase in the fluorescence quantum yield (up to 1%) and a red shift of the UV−vis absorption band with Archers being the most red-shifted.

Here, we applied rational design to perform further optimization of GEVIs from the Archers class. In previous studies, rational design approaches have not been applied systematically for the engineering of Arch-based GEVIs due to the lack of knowledge about the mechanisms that regulate fluorescence enhancement in these proteins. At this stage, a

Received: December 25, 2023
Revised: April 7, 2024
Accepted: April 8, 2024
Published: April 29, 2024

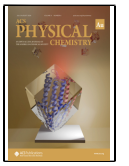

Table 1. Properties of Widely Applied Arch-Based GEVIs[a]

GEVI	λ_{max}, nm	λ_{em}, nm	fluorescence quantum yield, %	voltage sensitivity $\Delta F/F$ per 100 mV, %
QuasAr1	590[8]	715[8]	0.8[8]	32%[8]
QuasAr2	590[8]	715[8]	0.4[8]	90%[8]
Archon2	586[12]	735[12]	1.05[12]	20%[11]
NovArch	584[13]	725[13]	n/a	41%[14]
Archer1	626[10]	731[10]	0.33[10]	85%[9]
Arch-5	622[10]	731[10]	0.87[10]	n/a
Arch	556[7]	687[7]	0.01[10]	40%[7]

[a] λ_{max}—absorption band maximum, λ_{em}—fluorescence band maximum, voltage sensitivity is measured as the relative change of fluorescence intensity per 100 mV voltage step.

heuristic role of directed evolution methodology can be engaged. Specifically, directed evolution studies provided a substantial number of primary structures that correspond to either bright or dim Arch variants. These two sets can be used as a base for a subsequent comparative investigation in order to evaluate structure−property relationships required for a further rational design step. Following this line, we performed such comparative investigation of bright Arch mutants, Archers, obtained by directed evolution in the previous study ref 10 and the wild-type Arch. Resonance Raman, UV−vis, and fluorescence spectroscopy, along with computational modeling, were employed. We found that the key structural difference between bright Arch variants and the dim wild-type protein is the protonation states of two coupled titratable residues: the counterion D222 and the E214 residue of the proton release group. These findings allowed us to employ the rational design strategy and to propose new Arch-based GEVIs with red-shifted absorption bands (λ_{max} up to 640 nm) and enhanced fluorescence (quantum yield up to 0.97%).

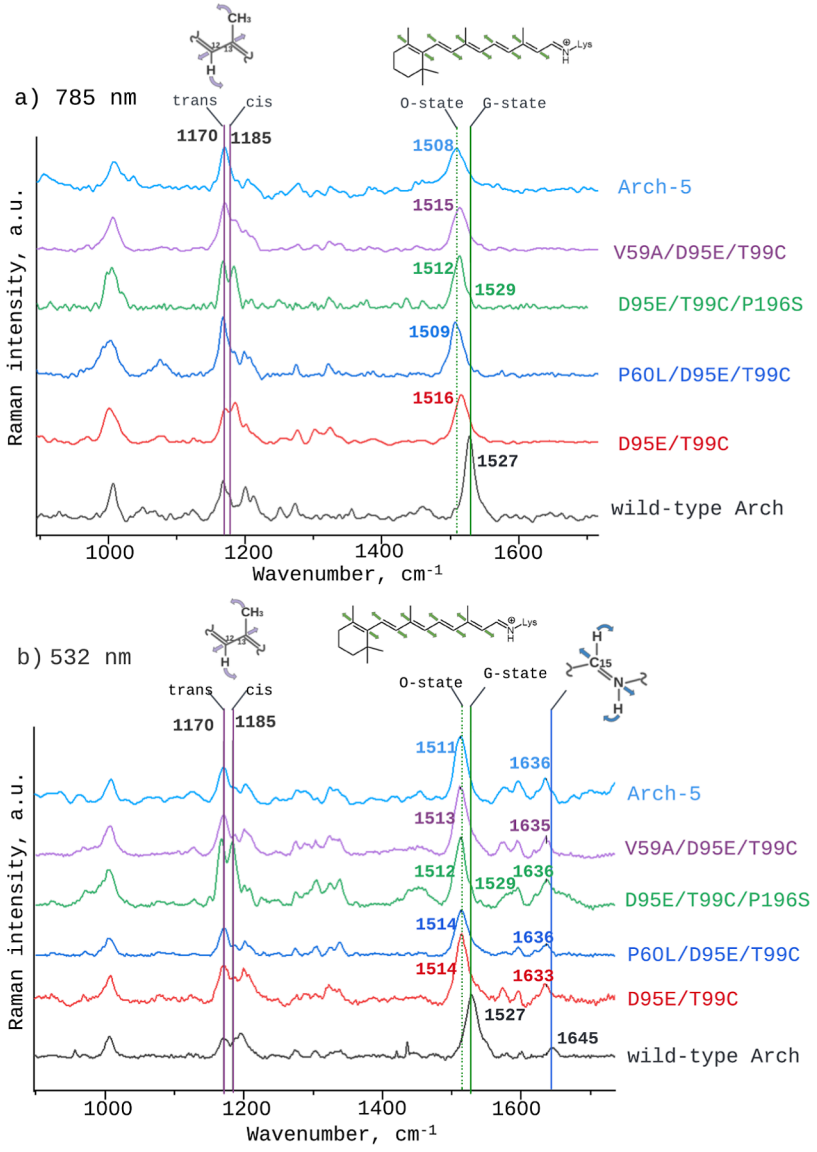

Figure 1. Resonance Raman spectra of the wild-type Arch and its bright variants. Purified samples were solubilized in 10 mM Tris, 200 mM NaCl, 0.15% DM, pH = 6.5. Raman spectra were recorded with excitation at 785 nm [dark-adapted spectrum, (a)] and 532 nm [light-adapted spectrum, (b)]. The laser power was set to 100 mW. Arch-5 denotes Arch V59A/P60L/D95E/T99C/P196S.

https://doi.org/10.1021/acsphyschemau.3c00073
ACS Phys. Chem Au 2024, 4, 347−362

Table 2. Light-Adapted and Dark-Adapted UV/Vis and Raman Spectral Bands' Absorption Maxima for Bacteriorhodopsin (bR) and Arch and Their Photocycle Intermediates[a]

bR intermediate	λmax, nm	ethylenic stretch vibrations, cm^{-1}	C=NH stretch vibrations, cm^{-1}	fingerprint vibrations, cm^{-1}
bR, light-adapted (G-state)	570[15] (565[20])	1528[15] (1527[20])	1640[15] (1641[20])	1168, 1185[15] (1167, 1184[20])
bR, dark-adapted	548[16] (557[21])	1536[16]	1634[16]	1168, 1182[16]
K	610[17]	1517[17]	1624[15]	1170, 1188[15]
L	550[15]	1539, 1551[15]	1645[15]	1169, 1188[15]
M	412[18]	1566[18]	1620[18]	1180, 1196[18]
N	560[19] (550[20])	1532, 1548[19]	1643[19]	1172, 1188[19]
O	640[18]	1508[18]		1166, 1198[18]
Q	(570−580)[20]			
P	490[22] 445[23] 525[23]			

[a]The values for Arch are given in parentheses. K, L, M, N, O denote intermediates of the main bR photocycle shown in Figure 2a. Q is the photocycle intermediate generated upon photoexcitation of the N intermediate.[20,21] P is the photocycle intermediate generated upon photoexcitation of the O intermediate.[22].

2. RESULTS AND DISCUSSION

In the first part of the "Results and Discussion" section, we start with our comparative experimental and computational investigation of the wild-type Arch and the set of bright Archers obtained by directed evolution in ref 10, i.e., D95E/T99C, P60L/D95E/T99C, V59A/D95E/T99C, D95E/T99C/P196S, and Arch-5, which is an abbreviation for V59A/P60L/D95E/T99C/P196S mutant. In the second part, we turn to the rational design and investigation of the new Arch variants.

2.1. Comparative Investigation of Archers and the Wild-type Arch

2.1.1. Resonance Raman Spectroscopy. Resonance Raman spectroscopy is a useful tool to evaluate the structural difference between rhodopsins. Resonance Raman spectroscopy can provide both direct information about intrinsic properties of the chromophore, e.g., *cis*- or *trans*-isomerism as well as indirect information about whole protein structure, e.g., Raman spectra contain information about the electrostatic field generated by the protein matrix in the chromophore binding pocket region and about hydrogen bonds that the surrounding amino acid or water molecule can form with the NH part of the chromophore.

Recorded light-adapted (532 nm probe) and dark-adapted (785 nm probe) Raman spectra of Arch and five investigated mutants are given in Figure 1. For interpretation of these spectra, we used previously reported[15−19] assignments of Raman spectral bands for the ground state and main photocycle intermediates of bacteriorhodopsin and Arch. These data are compiled in Table 2.

The bands with a maximum located in the 1508−1528 cm^{-1} region of Arch spectra can be assigned to the symmetric C=C ethylenic stretch mode. In full agreement with the previously reported data,[20] we found that the maximum of the C=C ethylenic stretch band ($\lambda_{C=C}$) of dark-adapted wild-type Arch Raman spectrum is located at 1527 cm^{-1} (see Figure 1). This value is just 1 cm^{-1} off of the corresponding bacteriorhodopsin ground state peak.[15] However, for all studied mutants, corresponding $\lambda_{C=C}$ bands for both dark- and light-adapted samples exhibit considerable red shifts from the wild-type Arch value. The observed red shift of the band maximum varies from 11 cm^{-1} for D95E/T99C to 19 cm^{-1} for Arch-5, making these value closer to the 1508 cm^{-1} reported for the bacteriorhodopsin O photocycle intermediate (O-state)[18] than to 1528 cm^{-1} of the ground state (G-state) conformation. In addition, a more careful inspection of this region in the Raman spectra of D95E/T99C/P196S revealed two peaks at −1529 and 1512 cm^{-1} that are close to the values of $\lambda_{C=C}$ of the bR G-state and the O-state, respectively.

The O-state is the last photocycle intermediate of many microbial rhodopsins that thermally converts back to the thermodynamically more stable ground state (G-state) on the millisecond time scale (Figure 2a). O-states possess substantially red-shifted absorption bands, e.g., λ_{max} = 640[24] and 556 nm[20] values were reported for the Arch O-state and G-state, respectively.

The ethylenic stretch vibrations frequencies for conjugated π-systems correlate with the bond length alternation (BLA) values[25,26] defined as the average of the difference between single and double bonds lengths along conjugated chain. Both these properties are well-known to be very sensitive to the electrostatic environment.[27−29] This fact allows us to attribute the observed red shift of the $\lambda_{C=C}$ band to the change of electrostatic field in the region of the retinal protonated Schiff base (PSB) due to the protonation of the D222 counterion. To get additional insights, we employed the results of our quantum mechanics/molecular mechanics (QM/MM) calculations. We calculated the BLA values for the chromophore geometries taken from the corresponding QM/MM G- or O-state models and plotted them against experimental $\lambda_{C=C}$ values as shown in Figure 3 (upper panel). For proteins with a single peak in the ethylenic stretch region, a clear linear correlation can be seen between BLA and $\lambda_{C=C}$ if one uses G-state model BLA values for the wild-type Arch and O-state model BLA values for the rest of the proteins. For D95E/T99C/P196S, the data also fit to the correlation line, if we attribute $\lambda_{C=C}$ = 1529 cm^{-1} to the G-state model and $\lambda_{C=C}$ = 1512 cm^{-1} to the O-state model.

Bands with maxima located in the 1633−1645 cm^{-1} region can be assigned to the C=N Schiff base stretch mode. In the Raman spectra of the considered Arch mutants, this band exhibits a small 6−9 cm^{-1} red shift relative to its position in the spectrum of the wild-type protein. This small shift can signify the change of the hydrogen bond network in the vicinity of the NH group of the chromophore that occurs when going from the G-to O-state. Indeed, as we found from analysis of our computational models for the G- and O-state of Arch (Figure 4), the hydrogen bond formed by the NH group and the closest water molecule becomes longer in the O-state model. This hydrogen bond elongation can provide a possible explanation for the observed red shift of the corresponding Raman band. To quantify this effect, we performed additional

https://doi.org/10.1021/acsphyschemau.3c00073
ACS Phys. Chem Au 2024, 4, 347−362

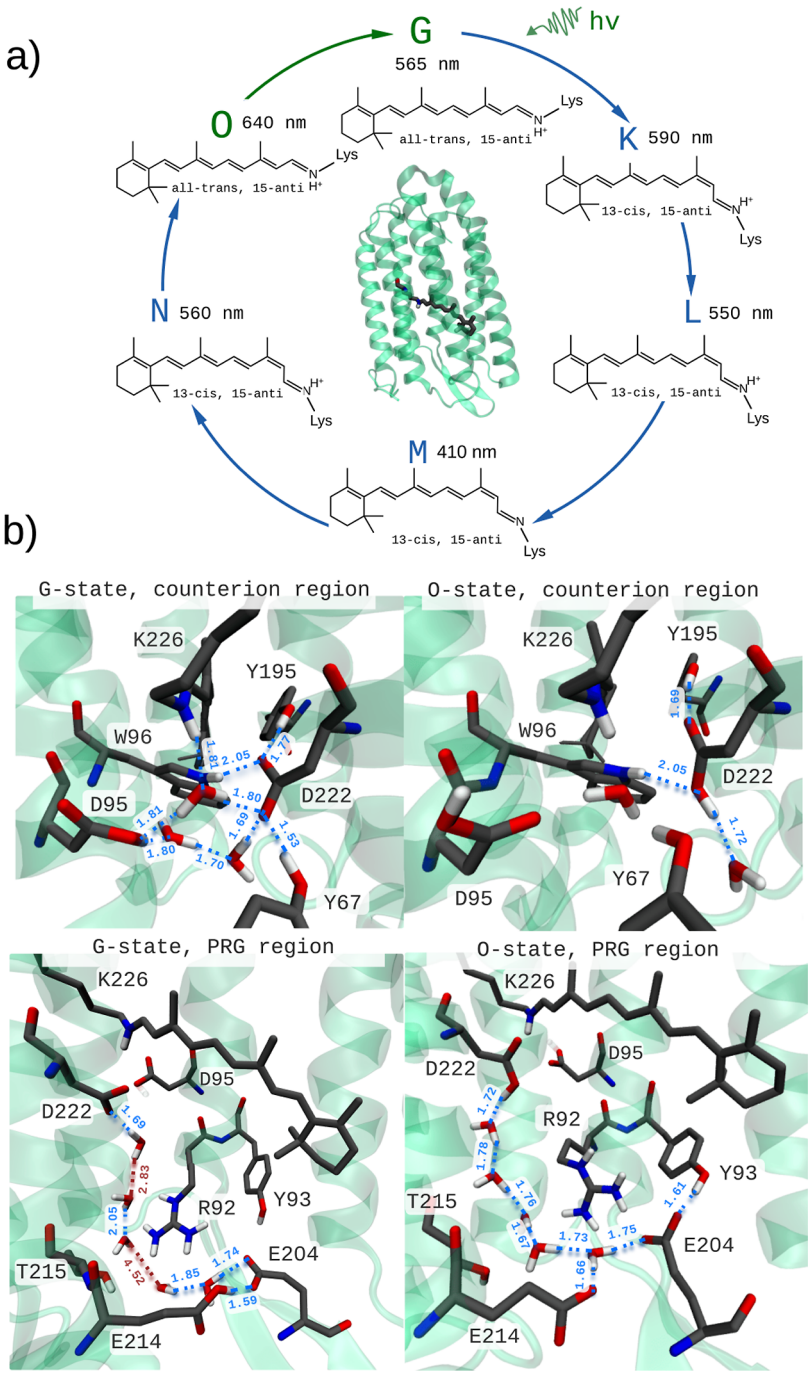

Figure 2. (a) Photocycle of the wild-type Arch. (b) Structures of the counterion region and the proton release group region in the G- and O-states of the wild-type Arch obtained from the corresponding QM/MM models. In the G-state, three water molecules are observed in the vicinity of D95 and D222 counterions. The D222 counterion is deprotontated, and it forms hydrogen bonds with Y67, Y195, W96, and two water molecules (upper left panel). E214 from the proton release group is protonated and forms a hydrogen bond with E207. The positively charged R92 is oriented toward T215 (lower left panel). In the O-state, only a single water molecule is observed in the vicinity of the counterions. D222 forms three hydrogen bonds with Y195, W96, and one water molecule located outside the counterion region (upper right panel). E214 is deprotonated, and E207 forms a hydrogen bond with Y93. The positively charged R92 is oriented toward negatively charged E214 and E207, giving space for the formation of a water chain between E214 and D222 (lower right panel).

calculations of vibrational frequencies using the cluster model approach as described in the "Materials and Methods" section. Our computational models give the 5 cm^{-1} red shift of the C=N Schiff base stretch band going from the G-to O-state model in good agreement with the 6−9 cm^{-1} red shift observed for Arch mutants in experiments.

The relative intensity of the bands located in the 1150−1300 cm^{-1} region, which is a structurally sensitive fingerprint region, reflects the ratio of 13-*cis* and all-*trans* isomers of the retinal chromophore.[30,31] The Raman spectra of all considered proteins suggest an equilibrium between these two isomers. The all-*trans* isomer dominates in both dark-adapted and light-adapted states of all proteins except for the dark-adapted state

https://doi.org/10.1021/acsphyschemau.3c00073
ACS Phys. Chem Au 2024, 4, 347−362

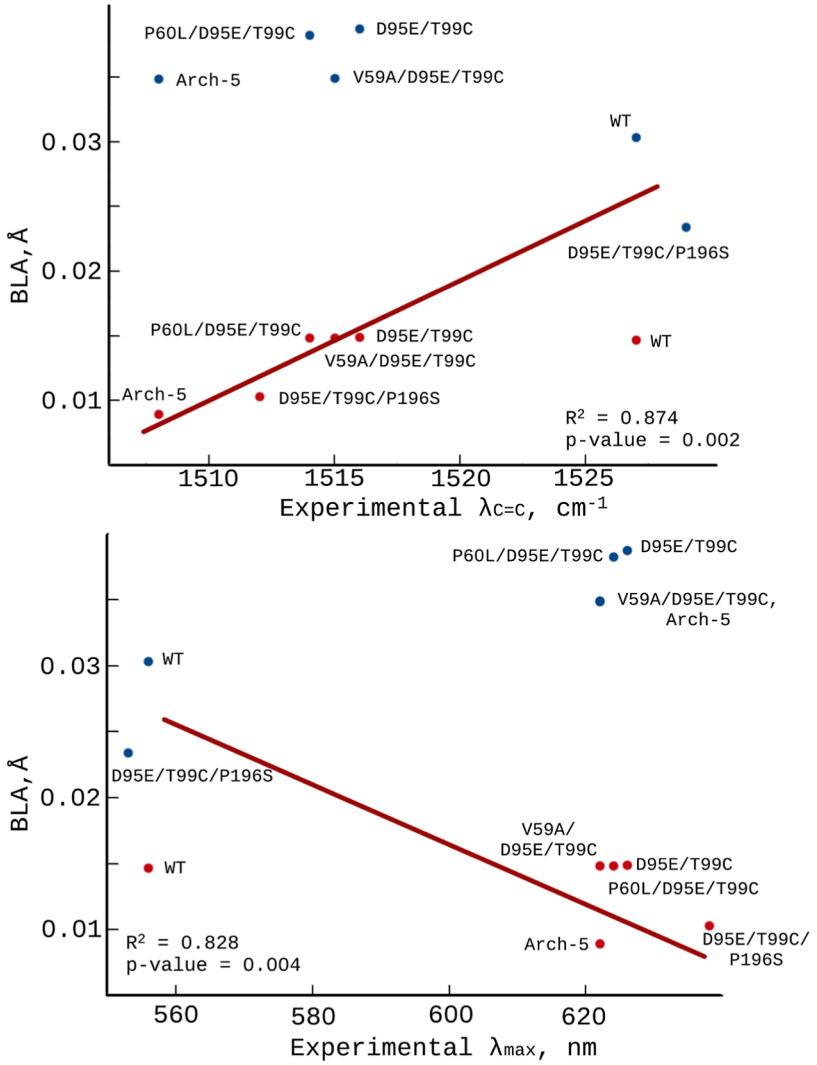

Figure 3. Bond length alternation of the chromophore (QM/MM models) versus experimental ethylenic stretch band maxima ($\lambda_{C=C}$, upper diagram) and absorption band maxima (λ_{max}, lower diagram). Blue and red dots correspond to BLA values obtained from the G- and O-state QM/MM models, respectively. The data were fitted by the least-squares method (the red lines). Arch-5 denotes Arch V59A/P60L/D95E/T99C/P196S.

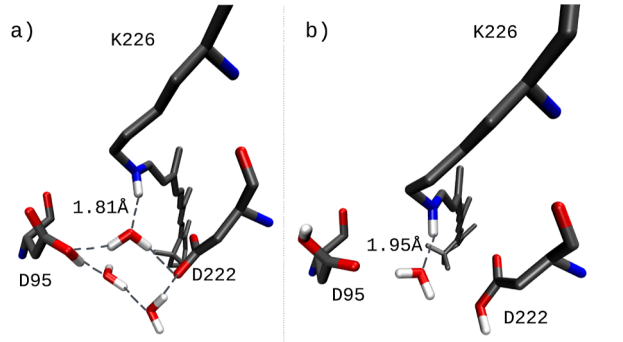

Figure 4. Cluster models employed to calculate the C=N Schiff base stretch mode vibration frequencies in the G- and O-states of the wild-type Arch. (a) Model for the G-state included the chromophore with K226 residue, D95, D222, and three water molecules. (b) Model for the O-state included the chromophore with K226 residue, D95, D222, and the single water molecule.

of D95E/T99C mutant, in which an increased concentration of the 13-*cis* isomer is observed.

2.1.2. UV–Vis Spectroscopy. Due to the charge-transfer character of the $S_0 \rightarrow S_1$ electronic transition in the PSB, UV–vis absorption band maxima of rhodopsins are very sensitive to the electrostatic field in the PSB region and can serve as a useful indicator for the presence and location of charged and/or polar residues in the protein structure. Therefore, a comparative analysis of UV–vis spectra of Archers and the wild-type Arch can support or, on the contrary, discard assumptions that have been made above based on our analysis of the Raman spectra.

Recorded UV–vis spectra for wild-type Arch and studied mutants are shown in Figure 5. The absorption maxima of these bands are also given in Table 3 along with the absorption band maxima obtained from the QM/MM calculations. The calculations were done both for G- and O-state models as described in the "Materials and methods" section. All experimental spectral bands can be perfectly fitted by a single Gaussian function except the spectral band of the D95E/T99C/P196S mutant, which clearly requires two Gaussian functions to be represented (for details, see Figure S2 in the Supporting Information).

https://doi.org/10.1021/acsphyschemau.3c00073
ACS Phys. Chem Au 2024, 4, 347–362

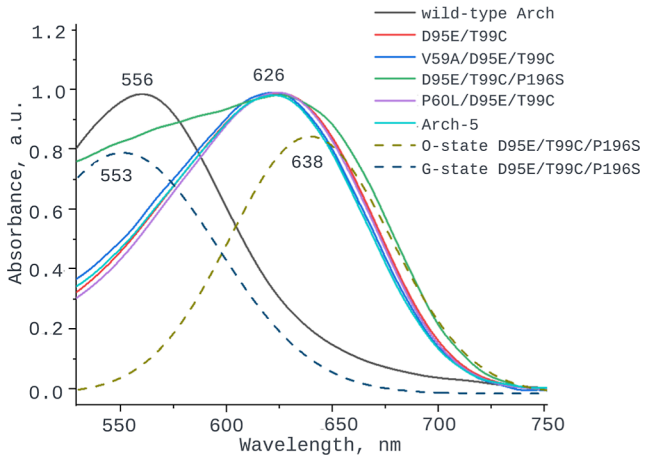

Figure 5. UV−vis absorption spectra of the wild-type Arch and its bright variants. Purified samples were solubilized in 10 mM Tris, 200 mM NaCl, 0.15% DM, pH = 6.5. The result of decomposition of the Arch D95E/T99C/P196S absorption band into two Gaussian functions is depicted as dotted lines.

The spectral bands for all mutants are considerably red-shifted relative to the wild-type Arch and are closer to λ_{max} = 640 nm reported for the O-states of bR[18] and Arch[24] than to λ_{max} = 565 nm of the wild-type Arch.[20] Similar to the Raman ethylenic stretch band discussed above, λ_{max} values calculated for the G-state models are in better agreement with experimental λ_{max} for Arch than the ones calculated for the O-state models. Also, experimental λ_{max} of D95E/T99C, P60L/D95E/T99C, V59A/D95E/T99C, and V59A/P60L/D95E/T99C/P196S mutants are better reproduced by the O-state models than by the G-state models. For D95E/T99C/P196S with two peaks observed experimentally, the G- and O-state models reproduced blue-shifted and red-shifted λ_{max} values, respectively. In addition, we found a correlation between experimental λ_{max} and calculated BLA values (Figure 3, lower panel).

In Figure 6, we compiled Arch and Archers' $\lambda_{C=C}$ and λ_{max} values obtained in this study together with available literature data for ground- and O-states of other microbial rhodopsins. Two distinct clusters can be identified: a cluster that includes wild-type microbial rhodopsins in their ground states and a cluster that includes O-states of microbial rhodopsins and studied bright Arch mutants.

2.1.3. Fluorescence Emission Spectroscopy and Quantum Yields. We also recorded fluorescence excitation and emission spectra and measured fluorescence quantum yields for all of the studied mutants. For D95E/T99C and D95E/T99C/P196S, the spectra are presented in Figure 7. The spectra for the rest of the mutants are similar to the D95E/T99C spectra and can be found in the Supporting Information (Figure S1). Maxima of fluorescence excitation bands, maxima of fluorescence emission bands, and fluorescence quantum yields are given in Table 3. Measured fluorescence emission maxima and quantum yields are in full agreement with previously reported values.[10] For Arch D95E/T99C, we have measured the fluorescence quantum yield value using the Quanta-ϕ integrating sphere of the Fluorolog-3 spectrofluorimeter. For other Arch variants, we used a comparative method with Arch D95E/T99C serving as a reference (see the Materials and Methods section). For the wild-type protein, we could not obtain confident values due to the extreme dimness of its fluorescence. The absorption maxima values of all considered mutants, except D95E/T99C/P196S, are almost identical to the corresponding fluorescence excitation maxima values (see Table 3), implying that the fluorescence arises from the absorbing form of the corresponding protein, and no other photocycle intermediates are involved. A similar observation has been previously reported

Table 3. Absorption Maxima (λ_{max} abs), Fluorescence Excitation Maxima (λ_{max} exc), Fluorescence Emission Maxima (λ_{max} em), Fluorescence Quantum Yield (QY), and Potential-Dependence of the Wild-type Arch and Arch Mutants Considered in This Study[a]

	experimental					calculated	
protein	λ_{max} abs, nm	λ_{max} exc, nm	λ_{max} em, nm	QY, %	Pot. dep	λ_{max} G-state, nm	λ_{max} O-state, nm
wild-type	556 (this study) 557, DA[20]						
	565, LA[20]		687[7]	0.01[10]		568 (trans) 557 (cis)	634
D95E/T99C	626	627	729	0.33 (this study and [10])	yes	548	621
P60L/D95E/T99C	624	625	725	0.40 (this study and [10])	yes	548	621
D95E/T99C/P196S	628 (553/638)	639	733	0.56 (this study and [10])	yes	564	639
V59A/D95E/T99C	622	623	724	0.62 (this study and [10])	yes	542	625
Arch-5	622	627	745	0.87 (this study and [10])	yes	558	626
Y195F	543/643	638	730	0.23	no	545	638
W96F	537					550	623
W96F/T215A	553/625	639	732	0.25	no	552	622
D95E/T99C/P196S/T215A	638	639	734	0.97	yes	578	640
D95E/T99C/T215A/A225M	640	640	737	0.77	yes	580	643

[a]Emission spectra were recorded with excitation at λ = 630 nm. Arch-5 denotes the quintuple mutant of Arch (V59A, P60L, D95E, T99C, P196S). For the wild-type Arch, we provide the λ_{max} values measured for dark-adapted (DA) and light-adapted (LA) proteins in the study ref 20.

https://doi.org/10.1021/acsphyschemau.3c00073
ACS Phys. Chem Au 2024, 4, 347−362

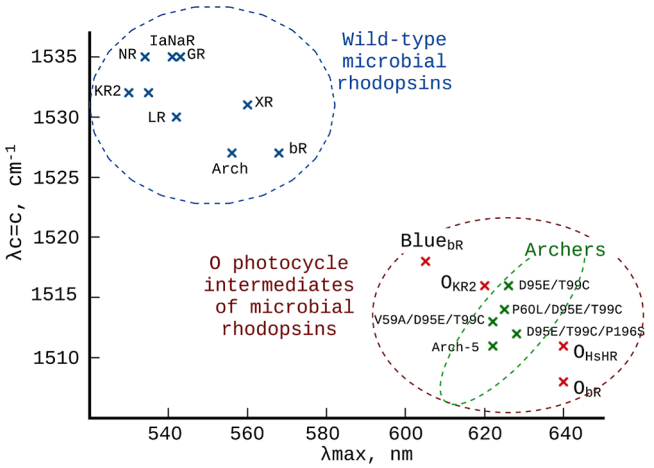

Figure 6. Ethylenic stretch band maxima of Raman spectra ($\lambda_{C=C}$) versus absorption band maxima of UV−vis spectra (λ_{max}) for microbial rhodopsins. Wild-type microbial rhodopsins are shown as blue dots. O photocycle intermediates of microbial rhodopsins and the blue form of bacteriorhodopsin are shown as red dots. Archers are shown as green dots. Abbreviations: KR2, *Krokinobacter* rhodopsin 2;[32] NR, *Neurospora rhodopsin*;[33] PspR, *Pseudomonas putida* rhodopsin;[34] IaNaR, *Indibacter alkaliphilus* rhodopsin;[35] GR, *Gloeobacter rhodopsin*;[36] LR, *Leptosphaeria rhodopsin*;[37] Arch, archaerhodopsin-3; XR, Xanthorhodopsin;[38] bR, light-adapted *Halobacterium salinarum* bacteriorhodopsin;[39] Blue$_{bR}$, the blue form of bR at pH = 2.6;[39] O$_{KR2}$, the O intermediate of KR2 photocycle;[40] O$_{HsHR}$, the O intermediate of *Halobacterium salinarum* halorhodopsin photocycle;[41] O$_{bR}$, the O intermediate of bR photocycle;[18] Arch-5, Arch V59A/P60L/D95E/T99C/P196S.

for QuasAr1 and QuasAr2.[8] Fluorescence in the wild-type Arch, conversely, arises through sequential action of three photons.[24] The D95E/T99C/P196S fluorescence excitation maximum was found to be 639 nm, which is in line with the observation that UV−vis spectral band of this protein can be fitted by two Gaussians (553 and 638 nm).

No evidence exists that the ground state of bR or Arch exhibits substantial fluorescence under physiological pH. On the contrary, the O-state of bR and other microbial rhodopsins have been reported to exhibit significant fluorescence emission.[21,42,43] High fluorescence was also detected for bR under low pH (blue form of bR).[44] For proteorhodopsin and bR, counterion protonation was shown to decrease the efficiency of PSB photoisomerization.[45,46] Apparently, neutralization of a negative charge in the NH region is an important condition that allowed the formation of bright fluorescent Archers. It is also worth mentioning here that the available experimental data, which are compiled and analyzed in our very recent review on fluorescent properties of both microbial and animal rhodopsins,[47] suggest that this statement is much more general and goes far beyond the Archers studied here.

2.1.4. pK_a Values of the Key Titratable Residues and PSB. One of the key factors that determine the nature of G- and O-states of microbial rhodopsins is the protonation state of the counterion (D212 in bR numbering) and the proton release group residue (E204 in bR numbering).[48,49] Specifically, D212 is deprotonated in the G-state and protonated in the O-state, while E204 is protonated in the G-state and deprotonated in the O-state. The proton transfer between E204 and D212 through a water chain, which connects these two residues, leads to transition from one state to another (see refs 49 and 50 and the subsection "QM/MM Models. Structural Analysis Of G- And O-States"). Another important indicator, which determines potential-dependence of the fluorescent signal and its sensitivity is the pK_a value of the chromophore (see ref 24 and the subsection "Prerequisites for Rational Design of New Bright Arch GEVIs"). Keeping it in mind, we applied spectrophotometric titrations to determine pK_a values of counterion D222, proton release group residue E214, and PSB of the wild type Arch and studied fluorescent mutants.

Measured pK_a values are given in Table 4, and titration curves can be found in the Supporting Information (Figures S4 and S5). While for D222 and PSB, transition from the protonated to deprotonated form is easily detectable by spectroscopy, the evaluation of such transition for E214 is challenging due to insufficient sensitivity of UV−vis spectrum to its protonation. Only for two proteins were we able to detect a small spectral band shift that can be attributed to E214 protonation. This low λ_{max} sensitivity to the change of E214 charge can be understood if the position of this residue relative to the chromophore is taken into consideration. Although the considered residue is situated relatively close (≈11 Å) to the nearest PSB atom, the distance to both ends of the

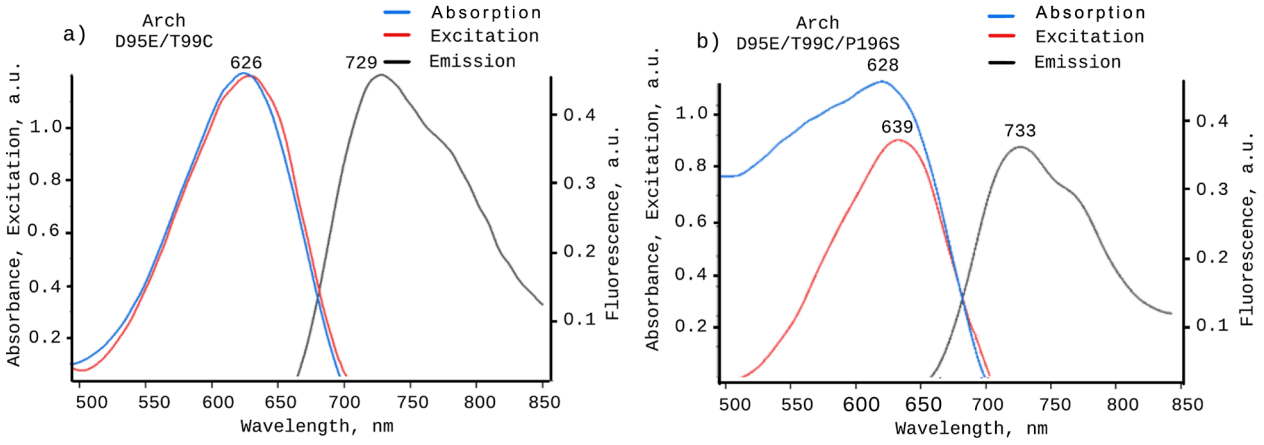

Figure 7. Absorption, excitation, and fluorescence emission spectra of Arch D95E/T99C (a) and Arch D95E/T99C/P196S (b). Purified samples were solubilized in 0.1% DM, 0.05 M Tris, 0.3 M NaCl, pH = 6.5. Excitation spectra were obtained with λ_{em} = 740 nm. Fluorescence emission spectra were obtained with λ_{exc} = 630 nm.

https://doi.org/10.1021/acsphyschemau.3c00073
ACS Phys. Chem Au 2024, 4, 347−362

Table 4. pKa Values of PSB, the D222 Counterion, E214 Residue of the Proton Release Group, and Potential Dependence of the Fluorescent Signal (Pot. Dep.) of Considered Arch Mutants[a]

protein	pK_a (PSB)	pK_a (D222)	pK_a (E214)	Pot. dep
wild type	>11	2.5		
D95E/T99C	7.5	8.9		yes
P60L/D95E/T99C	7.7	>9		yes
D95E/T99C/P196S	7.4	7.8	7.0	yes
V59A/D95E/T99C	7.9	>9	4.5	yes
Arch-5	7.6	9.1		yes
Y195F	>10	3.7		no
W96F	>10	2.5		no
W96F/T215A	9.4	9.5		no
D95E/T99C/P196S/T215A	7.4	7.9		yes
D95E/T99C/T215A/A225M	7.5	8.0		yes

[a]Arch-5 denotes the quintuple mutant of Arch (V59A, P60L, D95E, T99C, P196S).

chromophore is similar. As demonstrated in previous computational studies (see, e.g.,[51]), a charged residue located in such region does not significantly affect λ_{max}. We also obtained these small or even negligible spectral shifts with QM/MM calculations (for details, see Table S2 in the Supporting Information).

For the wild-type Arch, the measured value of counterion D222 pK_a (2.5) indicates deprotonated state of D222 at physiological pH. Similar pK_a(D222) values have been reported previously.[20,52] For the rest of the proteins considered in this section (except D95E/T99C/P196S), pK_a(D222) values are around or above 9.0, indicating their protonation under physiological pH. For D95E/T99C/V59A, pK_a(E214) = 4.5 indicates the deprotonated state of this residue at pH = 7. Protonation of the D222 counterion and deprotonation of proton release group residue E214 are typical structural features of the O-state.[48,49] For D95E/T99C/P196S, pK_a(D222) = 7.8 and pK_a(E214) = 7.0 suggest the equilibrium between two states that differ in protonation of these two residues. This assumption is in line with the fact that for this protein we observed a double band in the UV−vis spectrum and splitting of the $\lambda_{C=C}$ band in the resonance Raman spectrum. Obtained experimental data show that pK_a(D222) and pK_a(E214) are coupled, and both residues cannot be protonated or deprotonated simultaneously at physiological pH. This observation is in line with previous findings that demonstrated strong pK_a coupling between a residue of counterion complex and a proton release group residue E204 in bR.[53,54] The measured pK_a of PSB does not change significantly among discussed fluorescent mutants varying from 7.4 to 7.9. For the wild-type Arch, pK_a of PSB was found to be > 11, in agreement with previously reported data.[10]

2.1.5. QM/MM Models. Structural Analysis of G- and O-States. We used computational modeling (QM/MM and Molecular Mechanics all-atom molecular dynamics simulations) both to interpret experimental data as described above and to get additional insights given below. We started from a structural analysis of the G- and O-states for Arch and the fluorescent mutants. As discussed above, the transition from the O- to G-state is accompanied by proton transfer from D222 to E214. In accordance, analysis of the reported X-ray structure (PDB entry 6GUX[55]) and our QM/MM models reveals that the key structural differences between O- and G-states are observed in two regions: the vicinity of the NH chromophore moiety and the vicinity of the so-called proton release group (Figure 2b) that consists of E204, E214, R92, Y93 surrounded by water molecules.[48] The proton transfer is accompanied by several important structural changes. The pentagonal cluster formed by D222, D95, and three water molecules, which is a typical structural feature of G-state of Arch and bR,[48] is disrupted in the O-state, and only a single water molecule is left in this region. E204, which is connected by a hydrogen bond with E214 in the G-state, reorients in the O-state, making a hydrogen bond with Y93. During transition from the G-to O-state, positively charged R92 reorients from T215 toward E204 and E214, stabilizing a negative charge of the proton release group cluster. The reorientation of R92 in the O-state allows the formation of a continuous water chain between D222 and E214. A similar structural reorganization has been reported previously for bR.[49,50,56,57]

Analysis of Archers QM/MM models reveals that the most prominent changes occur in the D222 region of the G-state models after introducing D95E/T99C mutations (Figure 8). Replacement of aspartic acid D95 by the bulkier glutamic acid E95's destroyed water cluster in the NH region of PSB and only one of three water molecules remain in this region. The

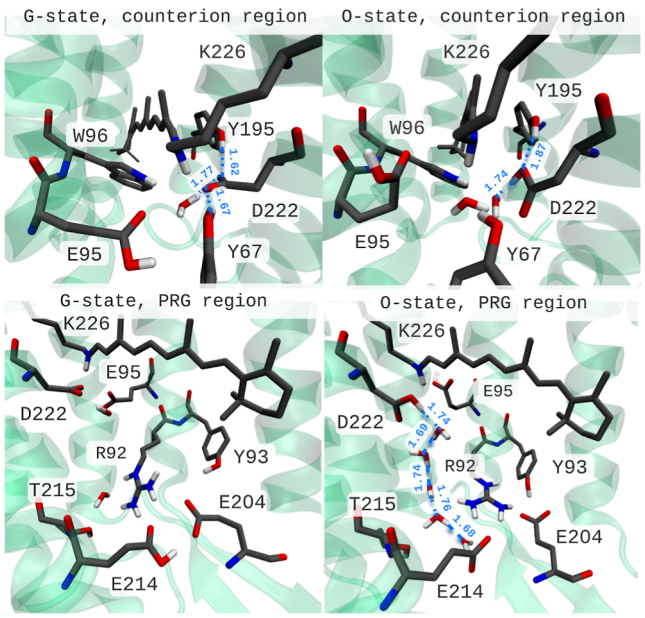

Figure 8. Structures of the counterion region and the proton release group region in the G- and O-states of the Arch D95E/T99C obtained from the corresponding QM/MM models. In the G-state, only a single water molecule is observed in the vicinity of E95 and D222 counterions. The D222 counterion is deprotonated, and it forms hydrogen bonds with Y67, Y195, and the water molecule from the counterion region (upper left panel). E214 from the proton release group is protonated and forms a hydrogen bond with E207. The positively charged R92 is oriented toward T215 (lower left panel). In the O-state, also only one water molecule is observed in the vicinity of the counterions. D222 forms two hydrogen bonds with Y195 and one water molecule located outside the counterion region (upper right panel). E214 is deprotonated, and E207 forms a hydrogen bond with Y93. The positively charged R92 is oriented toward negatively charged E214 and E207, giving space for the formation of a water chain between E214 and D222 (lower right panel).

https://doi.org/10.1021/acsphyschemau.3c00073
ACS Phys. Chem Au 2024, 4, 347−362

number of H-bonds formed by D222 with surrounding polar residues and water molecules decreased from 5 to 3, leading to increase of pK_a(D222) and, therefore, destabilization of the G-state. Apparently, such a structural change is the main reason for the observed alternation of the G- and O-state thermodynamic stability in bright Arch variants. For additional justification of this assumption, we developed Arch variants with alternative mutations that caused a similar structural reorganization. These new Arch variants are described in part 2 of the "Results and Discussion" section.

2.1.6. Molecular Dynamics Simulation of Structural Reorganization after the Proton Transfers between E214 and D222. We applied molecular dynamics simulations to investigate protein structure reorganization after E214 → D222 proton transfer for both the wild-type Arch and Archers. The corresponding G-state QM/MM structures were inserted into the lipid bilayer, and the obtained systems were hydrated, neutralized by adding Na^+ and Cl-ions, and equilibrated at T = 298 K and P = 1 atm as described in the "Materials and Methods" section. After the equilibration step, the proton located at the proton release group residue E214 was manually transferred to the counterion D222 and MD simulation continued until the system reached a new equilibrium. For all Arch mutants, MD simulations converged to a stable conformation within 8−15 ns, producing structures that are very similar to the corresponding O-state structures obtained with homology modeling [root-mean-square deviation (RMSD) in the range 0.6−0.9 Å]. On the contrary, for the wild type, Arch MD simulation did not converge to the O-state structure even after 70 ns, suggesting a high energy barrier for the G to O transition.

We also performed simulations starting from the O-state models following the same protocol. We equilibrated our O-state models in a membrane environment, manually transferred the proton from the counterion D222 to the proton release group residue E214, calculated a 70 ns MD trajectory, and analyzed the final structures by visual inspection. For all studied Arch mutants, after 70 ns, we did not detect any structural changes, suggesting a transition to the G-state. On the contrary, such a structural reorganization started to occur for the wild-type Arch. Specifically, we observed the formation of the hydrogen bond between proton release group residues E204 and E214, disruption of the continuous water chain from D222 to E214, and rotation of R92 residue from the proton release group toward T215. All of these structural changes were expected for the O-state → G-state transition. However, apparently, the length of trajectory was not enough, and we did not detect the final features that should indicate the formation of G-state, such as water cluster formation in the vicinity of the counterions.

2.2. Rational Design of New Arch Variants

2.2.1. Prerequisites for Rational Design of New Bright Arch GEVIs. Based on the investigation described in the previous section, we derived two prerequisites that allow us to obtain Archer variants with enhanced fluorescence conserving potential-dependence of the signal. Below, we describe these prerequisites.

2.2.1.1. Neutralization of the Counterions. In the previous part of the "Results and Discussion" section, we concluded that a substantial increase of the fluorescent signal can be achieved by an alteration of the G- and O-state stability. In Archers, such alteration is achieved by introducing two mutations, D95E and T99C. To test this statement further and to prove its generality, we proposed mutations other than D95E/T99C that can lead to the alteration of the G- and O-state stability and studied their fluorescence properties.

Two strategies to achieve the desired G- and O-state switching were applied: introducing substitutions to destabilize the G-state and vice versa and substitutions to stabilize the O-state. Two mutations, Y195F and W96F, were proposed to increase pK_a(D222) and, therefore, destabilize the G-state. Both of the polar residues Y195 and W96 form a hydrogen bond with D222 in the wild-type Arch, and their substitution by nonpolar phenylalanine will break this bond, leading to the pK_a(D222) increase (Figure 2b). However, since the H-bond Y195-D222 is noticeably stronger than that of W96-D222, the increase in pK_a(D222) was expected to be larger for the Y195F mutant. Indeed, in full agreement with our assumptions, measured resonance Raman, UV/vis, and fluorescence spectra (see Figure 9, Table 3, and Figure S3 in the Supporting Information) revealed a significant O-state mixture as well as significant increase of fluorescence (QY = 0.23%) for Y195F and only 1.5% O-state mixture and low fluorescent signal for the W96F mutant. It also worth mentioning here that the non-negligible ratio of the O-like state was also detected in previous studies for the bR Y185F mutant (Y185 position in bR corresponds to the Y195 position in archaerhodopsin-3).[52,58,59] For the W96F mutant, only slight fluorescence and a 1.5% O-state mixture were detected.

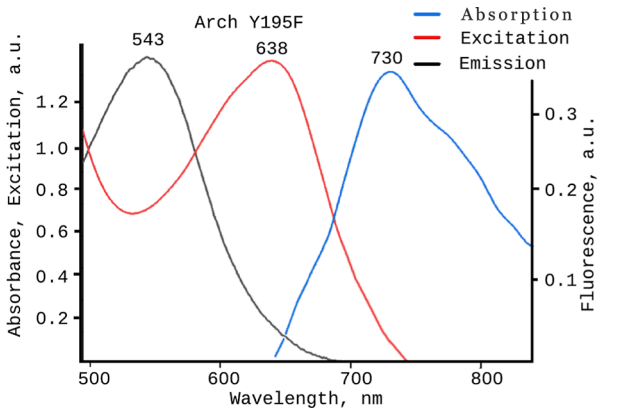

Figure 9. Absorption, excitation, and fluorescence emission spectra of Arch Y195F. The purified sample was solubilized in 10 mM Tris, 200 mM NaCl, 0.15% DM, pH = 6.5. An excitation spectrum was obtained with λ_{em} = 740 nm. A fluorescence emission spectrum was obtained with λ_{exc} = 630 nm.

In all fluorescent Arch mutants discussed previously, relative stability of G- and O-states was altered by destabilization of the G-state. Similar results can also be achieved by the O-state stabilization. To implement this strategy, we modified the W96F mutant by adding a T215A substitution. T215A mutation was selected based on the results of a previous experimental study,[60] in which introducing T215A mutation in bR was shown to increase O-state lifetime by 100 times compared to the wild-type protein. Indeed, analysis of resonance Raman and UV/vis spectra of the W96F/T215A mutant revealed a mixture of 30% O-state. W96F/T215A also demonstrates enhanced fluorescence (QY = 0.25%) compared to the wild-type Arch (Figure 10).

2.2.1.2. pK_a Value of PSB Is Important to Preserve Potential-Dependence of the Fluorescence. Our findings

https://doi.org/10.1021/acsphyschemau.3c00073
ACS Phys. Chem Au 2024, 4, 347−362

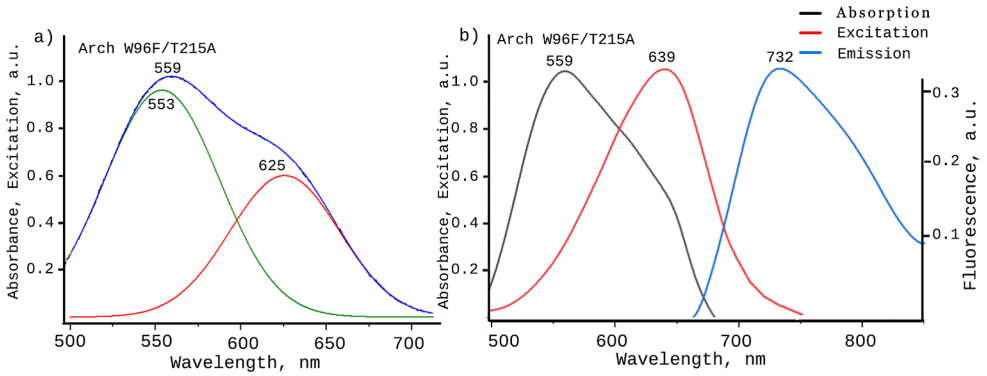

Figure 10. (a) Absorbance spectrum of purified Arch W96F/T215A solubilized in 10 mM Tris, 200 mM NaCl, 0.15% DM at pH = 6.5. The absorbance spectrum is fitted by two Gaussian functions attributed to the G-form and O-form of the protein. (b) Absorbance, fluorescence excitation, fluorescence emission spectral bands of Arch W96F/T215A recorded in 10 mM Tris, 200 mM NaCl, 0.15% DM at pH = 6.5.

reported in the previous section support the assumption that fluorescence enhancement in Arch-based sensors can be obtained by increasing the O-state/G-state ratio. However, we also found that fluorescence observed both in Y195F and W96F/T215A mutants was not potential-dependent. We evaluated pK_a values of PSB for Y195F and W96F/T215A by photometric titration and found them to be >10 and 9.4, respectively (Table 4), which is much higher than physiological pH and pK_a(PSB) values measured for above-discussed potential-dependent fluorescent Arch variants (≈7.5, Table 4). Apparently, to preserve voltage-dependence of a fluorescent signal, the pK_a value of the PSB should be close to physiological pH, and this statement should be considered as another important factor to keep in mind during rational design. This statement is in line with observations reported previously.[7,10] Moreover, a clear correlation between fluorescence voltage sensitivity and pK_a(PSB) is observed (see Figure 11 and Table 5).

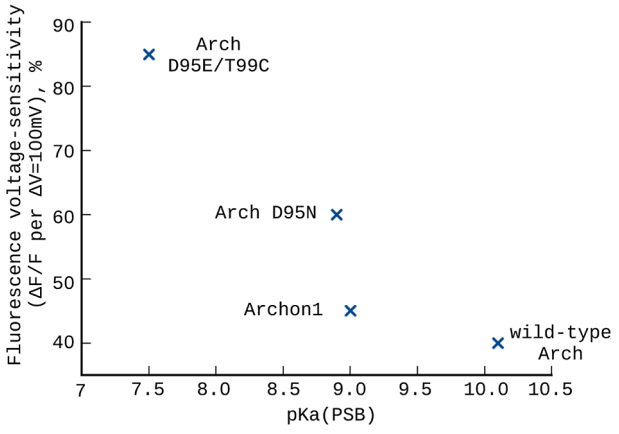

Figure 11. Fluorescence voltage sensitivity of Arch-based GEVIs measured as the relative change of fluorescence intensity on the 100 mV voltage change vs experimentally measured pK_a(PSB).

2.3. Rational Design of New Red-Shifted Bright Arch GEVIs

We used the principles formulated above to perform the rational design of new red-shifted bright Arch GEVIs. We chose to optimize red-shifting of λ_{max} not only due to practical importance of red-shifted variants for biomedical applications but also because a clear trend between λ_{abs} and fluorescence quantum yield was observed for microbial and animal

Table 5. Relationship between the Values of the Chromophore p*K*a and Voltage Sensitivity for Arch-Based GEVIs[a]

GEVI	pK_a (PSB)	voltage sensitivity $\Delta F/F$ per 100 mV (%)
Arch	10.1[7]	40[7]
Arch D95N	8.9[7]	60[7]
Archon1	~9[61]	40[11]
Archer1	7.5[10]	85[9]

[a]Voltage sensitivity is measured as the relative change of fluorescence intensity per 100 mV voltage step.

rhodopsins (see, e.g., a review[47]). According to the previous studies on electrostatic spectral tuning in rhodopsins (see, e.g., refs 51, 62 and 63), a spectral shift can be achieved by introducing, removing, or displacing/reorienting charged or polar residues. Effect of a charged/polar residue can be estimated based on the position of this residue relative to the chromophore.[51] Effect of polar residues is smaller, and non-negligible spectral shift can be achieved only for residues of the binding pocket. However, in the context of rational design, substitutions of polar residues is more preferable than substitutions of charged ones because introducing/removing of a charged residue can lead to a substantial H-bond network reorganization of a protein and subsequently to a substantial change of its properties including absorption band maxima.[62,63]

According to the data in Figure 5 of ref 51, introducing of polar residues in the vicinity of the six-membered ring of the chromophore can be used to achieve a red shift of UV−vis absorption band up to 15−20 nm. Such a substitution, namely, P196S, has been already introduced into Arch D95E/T99C in ref 10 and included in the set of bright Archers described above. However, the observed spectral shift was only 2 nm (Table 3).[10] At first glance, this negligible spectral shift contradicts the results of our QM/MM calculations that predicted a much larger 18 nm red shift [λ_{max}(O-state) values were 639 and 621 nm for D95E/T99C/P196S and D95E/T99C, respectively]. A more detailed analysis of the shape of the Arch D95E/T99C/P196S UV−vis absorption band reveals that it can be decomposed into two components with λ_{max} values of 553 and 638 nm (Figure 5), which are in good agreement with calculated λ_{max} values for G- and O-states of the protein (Table 3). Apparently, introducing P196S substitution into Arch D95E/T99C not only indeed red-shifted the O-form absorption band maximum up to ≈638 nm

https://doi.org/10.1021/acsphyschemau.3c00073
ACS Phys. Chem Au 2024, 4, 347−362

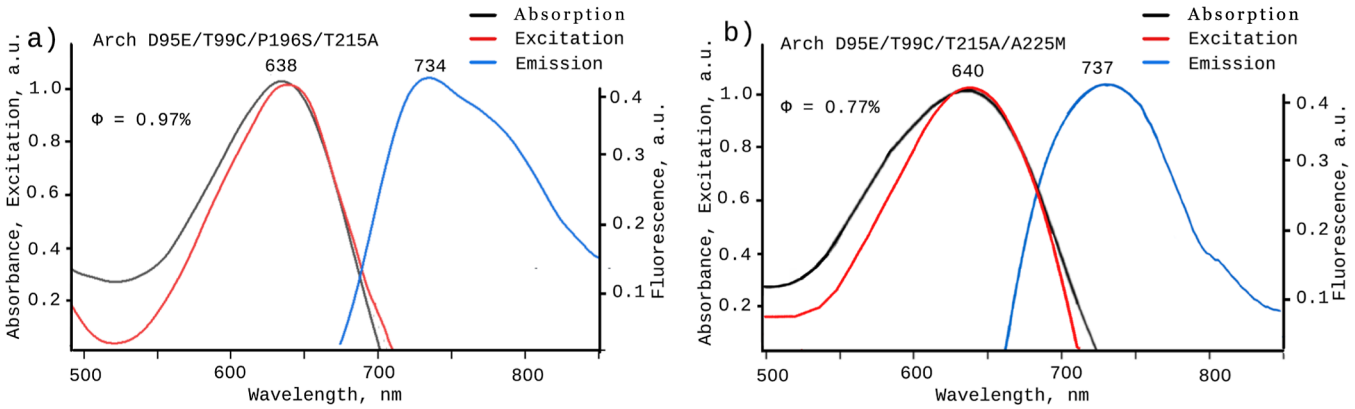

Figure 12. Absorption, excitation, and fluorescence emission spectra of Arch D95E/T99C/P196S/T215A (a) and Arch D95E/T99C/T215A/A225 M (b). Purified samples were solubilized in 0.1% DM, 0.05 M Tris, 0.3 M NaCl, pH = 6.5. Excitation spectra were obtained with λ_{em} = 740 nm. Fluorescence emission spectra were obtained with λ_{exc} = 630 nm.

but also caused a partial O-state destabilization. The substantial admixture of the G state with $\lambda_{max} \approx 553$ nm blue-shifts the overall spectrum to 628 nm. In line with the complex nature of the observed UV/vis band, the shapes and maxima of absorption and fluorescence excitation bands for this mutant are also different (Figure 7). Therefore, stabilization of O-form can lead not only to the red shift of absorption band maximum but also to the increase of fluorescence quantum yield at absorption band maximum wavelength. We introduced a T215A substitution into Arch D95E/T99C/P196S expecting stabilization of its O-state because such substitution allowed us to increase the thermodynamic stability of the O-state in the above-described Arch W96F. Indeed, the obtained quadruple mutant exhibits a UV/vis absorption band with λ_{max} = 638 nm. The fluorescence excitation spectrum of the D95E/T99C/P196S/T215A mutant is almost identical to the corresponding absorption band (Figure 12a). The fluorescence quantum yield at absorption band maximum wavelength has also increased from 0.56 to 0.97% after insertion of T215A substitution. It is important to notice that the obtained mutant conserved potential-dependence of the fluorescence signal, and we also showed that its pK_a(PSB) value (7.4) is located in the region characteristic for high voltage sensitivity (see Figure 11).

For additional verification of our design strategy, we considered another Archer mutant (Arch D95E/T99C/A225M abbreviated as Archer2), which was originally reported in ref 9 We synthesized this mutant and investigated its spectral properties. The absorption band of this protein can be decomposed into two Gaussian functions with $\lambda_{max} \approx 573$ and 649 nm, which can be attributed to the G- and O-states of the protein, respectively. Our QM/MM model of the O-state of this protein gives a similar λ_{max} value, 643 nm. Apparently, A225M substitution leads to a red shift of absorption band maximum. We also analyzed the QM/MM model to understand the spectral tuning mechanism provided by substitution of alanine located above the C13-Me group of the chromophore by bulkier methionine. We found that the spectral tuning is indirect, i.e., the influence on λ_{max} comes, at least partially, due to reorganization of residues other than substituted ones. Three effects were observed: 1) the distortion of the chromophore (the $C_{15}-C_{14}-C_{13}-C_{12}$ dihedral angle value changes from 172 to 165°); 2) the increase of distance between D95 and D222 counterions and the NH-group of the chromophore; 3) replacement of a water molecule, which is located above the C13-Me group of the chromophore in D95E/T99C by the side chain of M225.

Introducing the T215A mutation for O-state stabilization of the O state in Archer2 shifted the UV/vis absorption band λ_{max} value to 640 nm (Figure 12b) and increased the ratio of O-state. However, for this protein, O-state stabilization was not complete and an observable admixture of the G-state still persisted. Similar to Arch D95E/T99C/P196S/T215A, we observed a moderate increase of fluorescence quantum yield at absorption band maximum wavelength from 0.66 to 0.77%. We also confirmed that the potential-dependence of the fluorescence signal is conserved for the obtained mutant and showed that its pK_a(PSB) value (7.5) is located in the region characteristic of high voltage sensitivity (see Figure 11). The measured characteristics of proposed mutants can be found in Tables 3 and 4 and the Supporting Information (Figures S6 and S7).

To perform additional evaluation of fluorescence voltage sensitivity of new Arch mutants, we compared the *Escherichia coli* killing-induced fluorescence changes of the new proteins and Arch D95E/T99C, for which voltage sensitivity was previously measured in eukaryotic cells.[9] The relative change of fluorescence intensity upon the 100 mV voltage change ($\Delta F/F$ per 100 mV) reported in ref 9 is 85% (pH = 7.4). In our experiments, the relative changes of fluorescence upon killing *E. coli* cell (pH = 7.4) were found to be 1.2 and 1.6 times larger for Arch D95E/T99C/T215A/A225 M and Arch D95E/T99C/P196S/T215A, respectively, than for Arch D95E/T99C. Based on these values, we can suggest that new mutants exhibit higher voltage sensitivity than D95E/T99C, and their relative change of fluorescence intensity upon the 100 mV voltage change may exceed 100%.

3. CONCLUSIONS

Enhancement of the fluorescent signal and red-shifting of the absorption band maximum for rhodopsin-based genetically encoded voltage indicators are important to increase the applicability of these molecular instruments. Although recently reported natural rhodopsin, NeoR,[64,65] exhibits remarkable quantum yield of 20% and a far-red absorption band maximum at 690 nm, it can be considered only as a motivation for development of new efficient rhodopsin-based GEVIs but, due to the absence of potential dependence of its fluorescence signal, it cannot complement the available GEVI toolkit

https://doi.org/10.1021/acsphyschemau.3c00073
ACS Phys. Chem Au 2024, 4, 347−362

without further modification.[64] On other hand, designed voltage-dependent rhodopsins that were designed to be reported now exhibit much more modest fluorescence quantum yields, up to 1% (Table 1). Moreover, absorption band maxima of these proteins are still located far from the first biological window. Namely, for representatives of two of the three most widely used classes, QuasArs and Archons, λ_{max} values are situated in the 585−590 nm region (Table 1). Absorption bands of Arch-based GEVIs from the third class, Archers, are located in the far-red region (622−633 nm), which is more optimal for biological applications but still leaves room for improvement.

In this study, for GEVIs from the Archers class, we have achieved an additional red shift of absorption band maxima up to 640 nm (Table 3) and enhancement of the fluorescence quantum yield up to 0.97%, retaining voltage-dependence of the fluorescence signal at the same time. To our knowledge, obtained Arch-based GEVIs with λ_{max} = 640 nm are the most red-shifted GEVIs reported up to now. The obtained fluorescence quantum yield of 0.97% is the largest among Archers and comparable to quantum yields reported for Archons (1.05%, Table 1). We expect that both proposed new GEVIs and formulated design principles can be used in further studies: for voltage imaging research and for improvement of existing rhodopsin-based GEVIs, respectively.

In addition, our study highlights the sometimes underestimated heuristic potential of directed evolution approaches. If the goal is to optimize a certain property, for which defining factors are unknown, application of the directed evolution approach allows us not only to obtain proteins with desired properties but also gives a set of objects for further investigation that can help to elucidate these factors.

4. MATERIALS AND METHODS

A detailed description of the experimental and computational methods is given in the Supporting Information. Below, we provide a brief summary of applied protocols.

4.1. Sample Preparation and Spectroscopy

Wild-type Arch and its mutants were expressed in *E. coli* cells, prepared according to the protocol described previously,[8] and solubilized in a buffer containing 0.1% *n*-Decyl-*β*-D-maltopyranoside (DM), 0.5 M 4-(2-hydroxyethyl)-1-piperazineethanesulfonic acid, 0.3 M NaCl. Dark-adapted and light-adapted UV/vis spectra of purified proteins solubilized in Tris buffer (10 mM Tris, 200 mM NaCl, 0.15% DM, pH = 6.5) were recorded at room temperature on a NanoDrop 2000c spectrophotometer (Thermo Fisher Scientific).[10] Dark-adapted samples were prepared by incubation in the dark for 1 h prior to the measurements. Light-adapted samples were obtained by illumination with a 5 mW 532 nm laser for 10 min immediately before the measurements.[20] Sample size was 300 μL in all measurements. Resonance Raman spectra of purified proteins solubilized in Tris buffer (sample size 300 μL) were recorded at room temperature on the express-Raman spectrometer SENTERRA (Bruker) equipped with a 50× objective using 100 mW 785 nm and 40 mW 532 nm excitations. Fluorescence excitation and emission spectra were recorded using a Fluorolog-3 spectrofluorometer (Horiba Jobin Yvon) on purified protein samples solubilized in the Tris buffer (sample size 300 μL).

4.2. Fluorescence Quantum Yield and Potential-Dependence of Fluorescence Measurement

For Arch D95E/T99C, a fluorescence quantum yield measurement was performed using the Quanta-*ϕ* integrating sphere of Fluorolog-3. The obtained fluorescence quantum yield (0.33%) is in full agreement with the previously reported data.[10] For the rest of studied proteins, a comparative method with Arch D95E/T99C serving as a reference was applied.[8] Specifically, quantum yield measurements were performed on a series of dilutions of each protein solution and the reference with OD(λ_{max}) values 0.15, 0.1, 0.07, 0.05, and 0.03. For each dilution, the fluorescence emission spectrum was recorded with excitation at the absorption band maximum wavelength, and the total fluorescence intensities were obtained by integration. Fluorescence spectra were obtained on a Chirascan-plus spectrofluorometer (Applied Photophysics). For each measurement, the sample size was 300 μL. Integrated fluorescence intensity as a function of OD(λ_{max}) was plotted for each protein and the reference and approximated by a linear function. To derive fluorescence quantum yield values from the obtained slopes (S), the following equation was used: $\Phi_{protein} = \Phi_{D95E/T99C} \cdot (S_{protein}/S_{D95E/T99C})$. To evaluate the potential-dependence of fluorescence, the emission spectra were recorded from alive *E. coli* cells expressing Arch mutants and from the same cells after adding of kanamycin to the cell medium.[66] The observed raise of integrated fluorescence intensity after cell death was attributed to the potential-dependence of fluorescence.[61,67]

4.3. QM/MM Model Construction

The QM/MM model of the wild-type Arch was constructed starting from the corresponding X-ray structure (PDB entry 6GUX, 1.3 Å resolution).[55] To obtain G-state models of Arch mutants, O-state models, and blue form models of all considered proteins, the homology modeling approach was applied. The X-ray structures of the wild-type Arch, the bacteriorhodopsin L93A O intermediate (PDB entry 3VI0, 2.3 Å resolution, sequence identity to Arch 58%),[68] and the acid blue form of bacteriorhodopsin (PDB entry 1X0I, 2.3 Å resolution)[69] were used as templates for the construction of G-state, O-state, and blue form homology models, respectively. AlignMe 1.2[70] and I-TASSER 5.1[71] were employed for pairwise sequence alignments and construction of three-dimensional structures, respectively.[72] For O-state and blue form models, I-TASSER generated only a single model, which was used in subsequent calculations. For G-state models, I-TASSER generated two models. The structure of model1 was closer to the O-state model of the wild-type Arch than to its G-state; E204 residue from the proton release group was oriented toward Y93; positively charged R92 was oriented toward E207 and E214. On the other hand, the structure of model2 was closer to the G-state model of the wild type Arch — E207 and E214 residues of the proton release group formed the hydrogen bond; R92 was oriented toward T215. For this reason, model2 was selected for subsequent calculations.

At the next step, all models were complemented with the all-*trans* retinal chromophore, and water molecules in protein cavities were added with the Dowser++ program.[73] The pK_a values of titratable residues were determined with PropKa 3.1[74] complemented with parameters to take into account the electrostatics of the protonated retinal Schiff base during calculations (parameters are sent upon request). Hydrogen atoms were added to protein and water molecules with pdbpqr version 2.1.0.[75] Based on pK_a evaluation, standard protonation states at pH 7 (G-state and O-state models) and pH 2.6 (blue form models) were assigned to all residues. For QM/MM calculations, the B3LYP/6-31g*/Amber99 ASEC-FEG protocol[76−78] was employed as described in the Supporting Information Methods. The QM region included 48 atoms of retinal and the NH-$C_\varepsilon H_2$ moiety of K226, and the rest of protein atoms and water molecules were described at the MM level. The hydrogen link atom approach was employed for treating the interface between the QM and MM subsystems placed at the C_ε−C_δ bond of K226. QM/MM calculations were carried out with Molcas 7.2[79] interfaced to Tinker 5.1.[80]

4.4. Calculation of Absorption Maxima and Vibrational Frequencies

For calculation of the absorption maxima values, we used the above-described QM/MM ASEC-FEG models. The SORCI+Q(6,6)/6-31G* level of theory was employed to calculate energy of the $S_0 \rightarrow S_1$ vertical transition of the chromophore in the environment of the ASEC pseudoatoms' point charges. The ORCA 3.0.3[81] program package was used for these calculations.

https://doi.org/10.1021/acsphyschemau.3c00073
ACS Phys. Chem Au 2024, 4, 347−362

For calculation of vibrational frequencies of the C=N Schiff base stretch mode vibration, we employed cluster models. The models included the chromophore with K226, D95, and D222, three water molecules and the chromophore with K226, D95, and D222, one water molecule for the G-state and O-state models of the wild-type Arch, respectively. The geometry of each cluster was optimized, and vibrational frequencies in harmonic approximation were calculated at the B3LYP/6-31g* level of theory. The Gaussian 09 program was used for these calculations.[82]

4.5. MD for the Membrane-Embedded Models

To investigate protein structural changes that occur after a proton transfer between E214 and D222 residues, all-atom MD simulations for the corresponding proteins embedded in the membrane were carried out. To obtain the membrane-embedded models, the corresponding G-state or the O-state QM/MM model was inserted in the equilibrated box of a 1-palmitoyl-2-oleoyl-*sn*-glycero-3-phosphocholine (POPC) lipid bilayer. The system was hydrated and neutralized by adding Na^+ and Cl-ions using standard Gromacs tools. For the obtained system, energy minimization (maximum force threshold of 1000 kJ/mol/nm) was carried out followed by heating to 293 K and a 10 ns thermal equilibration in an *NVT* ensemble with position restraints applied on all heavy atoms (force constant of 1000 kJ/mol/nm). Then, the system was equilibrated in the *NPT* ensemble for 20 ns. At this stage, position restraints were applied only on backbone atoms, and their magnitude was sequentially decreased from 1000 kJ/mol/nm during the first 3 ns up to zero during the last 5 ns. To investigate protein structural changes that occur after a proton transfer between E214 and D222 residues, the proton was transferred from one position to another, and all-atom MD simulations were carried out. The analysis of MD trajectory was performed to detect structural reorganization as the change of the RMSD of protein heavy atoms and by visual inspection.

MD simulations were performed with Gromacs 2019.1[83] using Amber99sb force field[84] complemented with parameters for lipids[85] and all-*trans* retinal bound to lysine.[86] The integration step of 1 fs, 12 Å cutoff for van der Waals interactions and short-range electrostatics, and Particle Mesh Ewald summation[87] for long-range electrostatics were used in all simulations. The Nose–Hoover thermostat[88] and Parrinello–Rahman barostat[89] were used for controlling temperature and pressure, respectively. Visualization and analysis of molecular dynamics trajectories and protein structures were performed with VMD 1.9.4.[90]

■ ASSOCIATED CONTENT

Supporting Information

The Supporting Information is available free of charge at https://pubs.acs.org/doi/10.1021/acsphyschemau.3c00073.

Additional description of experimental protocols and computational methods; list of primers used to insert amino acid replacements, sequencing results; absorbance, fluorescence excitation, fluorescence emission spectral bands of considered Arch mutants; results of fitting of UV/vis absorption bands of considered Arch mutants with two Gaussian functions; resonance Raman spectra of Arch W96F and Y195F; titration curves obtained to determine pK_a(PSB) and pK_a(D222) of considered Arch mutants; calculated λ_{max} values for O-states and blue forms of Arch mutants; results of fluorescence quantum yield determination for Arch mutants; results of fluorescence potential-dependence measurements for Arch mutants (PDF)

QM/MM models for the wild-type Arch and considered Arch mutants; structures of the wild-type Arch and considered Arch mutants obtained after MD simulations; and results of calculation of C=NH stretch vibration frequency for G- and O-forms of wild-type Arch (ZIP)

■ AUTHOR INFORMATION

Corresponding Author

Mikhail N. Ryazantsev − *Institute of Chemistry, Saint Petersburg State University, St. Petersburg 198504, Russia;* orcid.org/0000-0003-3413-1706; Email: mikhail.n.ryazantsev@gmail.com, m.ryazantsev@spbu.ru

Authors

Dmitrii M. Nikolaev − *Institute of Chemistry, Saint Petersburg State University, St. Petersburg 198504, Russia; Institute of Biomedical Systems and Biotechnologies, Peter the Great St. Petersburg Polytechnic University, St. Petersburg 195251, Russia*

Vladimir N. Mironov − *Saint Petersburg Academic University, St. Petersburg 194021, Russia*

Ekaterina M. Metelkina − *Institute of Chemistry, Saint Petersburg State University, St. Petersburg 198504, Russia*

Andrey A. Shtyrov − *Institute of Chemistry, Saint Petersburg State University, St. Petersburg 198504, Russia*

Andrey S. Mereshchenko − *Institute of Chemistry, Saint Petersburg State University, St. Petersburg 198504, Russia;* orcid.org/0000-0001-9390-1446

Nikita A. Demidov − *Saint Petersburg Academic University, St. Petersburg 194021, Russia*

Sergey Yu. Vyazmin − *Saint Petersburg Academic University, St. Petersburg 194021, Russia*

Tatiana B. Tennikova − *Institute of Chemistry, Saint Petersburg State University, St. Petersburg 198504, Russia*

Svetlana E. Moskalenko − *Department of Genetics and Biotechnology, Saint Petersburg State University, St. Petersburg 199034, Russia; Vavilov Institute of General Genetics, St. Petersburg Branch, Russian Academy of Sciences, St. Petersburg 199034, Russia*

Stanislav A. Bondarev − *Department of Genetics and Biotechnology, Saint Petersburg State University, St. Petersburg 199034, Russia; Laboratory of Amyloid Biology, Saint Petersburg State University, St. Petersburg 199034, Russia;* orcid.org/0000-0003-3137-944X

Galina A. Zhouravleva − *Department of Genetics and Biotechnology, Saint Petersburg State University, St. Petersburg 199034, Russia; Laboratory of Amyloid Biology, Saint Petersburg State University, St. Petersburg 199034, Russia*

Andrey V. Vasin − *Institute of Biomedical Systems and Biotechnologies, Peter the Great St. Petersburg Polytechnic University, St. Petersburg 195251, Russia*

Maxim S. Panov − *Institute of Chemistry, Saint Petersburg State University, St. Petersburg 198504, Russia; St. Petersburg State Chemical Pharmaceutical University, St. Petersburg 197022, Russia*

Complete contact information is available at: https://pubs.acs.org/10.1021/acsphyschemau.3c00073

Notes

The authors declare no competing financial interest.

https://doi.org/10.1021/acsphyschemau.3c00073
ACS Phys. Chem Au 2024, 4, 347−362

■ ACKNOWLEDGMENTS

The study was funded by the Russian Science Foundation (RSF), grant no. 23-73-00041. The authors express their gratitude to the "Center for Molecular and Cell Technologies", "Center for Optical and Laser Research", "Center for Chemical Analysis and Materials Research", "Center for Magnetic Resonance" of Research park of Saint Petersburg State University. The authors also acknowledge computational resources of Peter the Great Saint Petersburg Polytechnic University Supercomputing Center (www.spbstu.ru). The research was carried out using the equipment of the shared research facilities of HPC computing resources at Lomonosov Moscow State University. This work is dedicated to the 300th anniversary of Saint Petersburg State University.

■ REFERENCES

(1) Lin, M. Z.; Schnitzer, M. J. Genetically encoded indicators of neuronal activity. *Nat. Neurosci.* **2016**, *19*, 1142−1153.
(2) Shen, Y.; Nasu, Y.; Shkolnikov, I.; Kim, A.; Campbell, R. E. Engineering genetically encoded fluorescent indicators for imaging of neuronal activity: Progress and prospects. *Neurosci. Res.* **2020**, *152*, 3−14.
(3) Azimi Hashemi, N.; Bergs, A. C.; Schüler, C.; Scheiwe, A. R.; Steuer Costa, W.; Bach, M.; Liewald, J. F.; Gottschalk, A. Rhodopsin-based voltage imaging tools for use in muscles and neurons of Caenorhabditis elegans. *Proc. Natl. Acad. Sci. U.S.A.* **2019**, *116*, 17051−17060.
(4) Xu, Y.; Zou, P.; Cohen, A. E. Voltage imaging with genetically encoded indicators. *Curr. Opin. Chem. Biol.* **2017**, *39*, 1−10.
(5) Nikolaev, D. M.; Mironov, V. N.; Shtyrov, A. A.; Kvashnin, I. D.; Mereshchenko, A. S.; Vasin, A. V.; Panov, M. S.; Ryazantsev, M. N. Fluorescence Imaging of Cell Membrane Potential: From Relative Changes to Absolute Values. *Int. J. Mol. Sci.* **2023**, *24*, 2435.
(6) Chow, B. Y.; Han, X.; Dobry, A. S.; Qian, X.; Chuong, A. S.; Li, M.; Henninger, M. A.; Belfort, G. M.; Lin, Y.; Monahan, P. E.; Boyden, E. S. High-performance genetically targetable optical neural silencing by light-driven proton pumps. *Nature* **2010**, *463*, 98−102.
(7) Kralj, J. M.; Douglass, A. D.; Hochbaum, D. R.; Maclaurin, D.; Cohen, A. E. Optical recording of action potentials in mammalian neurons using a microbial rhodopsin. *Nat. Methods* **2012**, *9*, 90−95.
(8) Hochbaum, D. R.; Zhao, Y.; Farhi, S. L.; Klapoetke, N.; Werley, C. A.; Kapoor, V.; Zou, P.; Kralj, J. M.; Maclaurin, D.; Smedemark-Margulies, N.; et al. All-optical electrophysiology in mammalian neurons using engineered microbial rhodopsins. *Nat. Methods* **2014**, *11*, 825−833.
(9) Flytzanis, N. C.; Bedbrook, C. N.; Chiu, H.; Engqvist, M. K.; Xiao, C.; Chan, K. Y.; Sternberg, P. W.; Arnold, F. H.; Gradinaru, V. Archaerhodopsin variants with enhanced voltage-sensitive fluorescence in mammalian and Caenorhabditis elegans neurons. *Nat. Commun.* **2014**, *5* (1), 4894−4899.
(10) McIsaac, R. S.; Engqvist, M. K.; Wannier, T.; Rosenthal, A. Z.; Herwig, L.; Flytzanis, N. C.; Imasheva, E. S.; Lanyi, J. K.; Balashov, S. P.; Gradinaru, V.; Arnold, F. H. Directed evolution of a far-red fluorescent rhodopsin. *Proc. Natl. Acad. Sci. U.S.A.* **2014**, *111*, 13034−13039.
(11) Piatkevich, K. D.; Jung, E. E.; Straub, C.; Linghu, C.; Park, D.; Suk, H.-J.; Hochbaum, D. R.; Goodwin, D.; Pnevmatikakis, E.; Pak, N.; et al. A robotic multidimensional directed evolution approach applied to fluorescent voltage reporters. *Nat. Chem. Biol.* **2018**, *14*, 352−360.
(12) Penzkofer, A.; Silapetere, A.; Hegemann, P. Absorption and emission spectroscopic investigation of the thermal dynamics of the Archaerhodopsin 3 based fluorescent voltage sensor Archon2. *Int. J. Mol. Sci.* **2020**, *21*, 6576.
(13) Mei, G.; Cavini, C. M.; Mamaeva, N.; Wang, P.; DeGrip, W. J.; Rothschild, K. J. Optical switching between long-lived states of opsin transmembrane voltage sensors. *Photochem. Photobiol.* **2021**, *97*, 1001−1015.
(14) Chien, M.-P.; Brinks, D.; Testa-Silva, G.; Tian, H.; Phil Brooks, F., III; Adam, Y.; Bloxham, B.; Gmeiner, B.; Kheifets, S.; Cohen, A. E. Photoactivated voltage imaging in tissue with an archaerhodopsin-derived reporter. *Sci. Adv.* **2021**, *7*, No. eabe3216.
(15) Lohrmann, R.; Stockburger, M. Time-resolved resonance Raman studies of bacteriorhodopsin and its intermediates K590 and L550: Biological implications. *J. Raman Spectrosc.* **1992**, *23*, 575−583.
(16) Smith, S. O.; Pardoen, J. A.; Mulder, P. P.; Curry, B.; Lugtenburg, J.; Mathies, R. Chromophore structure in bacteriorhodopsin's O640 photointermediate. *Biochemistry* **1983**, *22*, 6141−6148.
(17) Shim, S.; Dasgupta, J.; Mathies, R. A. Femtosecond time-resolved stimulated Raman reveals the birth of bacteriorhodopsin's J and K intermediates. *J. Am. Chem. Soc.* **2009**, *131*, 7592−7597.
(18) Ames, J. B.; Mathies, R. A. The role of back-reactions and proton uptake during the N .fwdarw. O transition in bacteriorhodopsin's photocycle: a kinetic resonance Raman study. *Biochemistry* **1990**, *29*, 7181−7190.
(19) Eisfeld, W.; Pusch, C.; Diller, R.; Lohrmann, R.; Stockburger, M. Resonance Raman and optical transient studies on the light-induced proton pump of bacteriorhodopsin reveal parallel photocycles. *Biochemistry* **1993**, *32*, 7196−7215.
(20) Saint Clair, E. C.; Ogren, J. I.; Mamaev, S.; Russano, D.; Kralj, J. M.; Rothschild, K. J. Near-IR resonance Raman spectroscopy of archaerhodopsin 3: effects of transmembrane potential. *J. Phys. Chem. B* **2012**, *116*, 14592−14601.
(21) Ohtani, H.; Tsukamoto, Y.; Sakoda, Y.; Hamaguchi, H. Fluorescence spectra of bacteriorhodopsin and the intermediates O and Q at room temperature. *FEBS Lett.* **1995**, *359*, 65−68.
(22) Popp, A.; Wolperdinger, M.; Hampp, N.; Brüchle, C.; Oesterhelt, D. Photochemical conversion of the O-intermediate to 9-cis-retinal-containing products in bacteriorhodopsin films. *Biophys. J.* **1993**, *65*, 1449−1459.
(23) Gillespie, N. B.; Wise, K. J.; Ren, L.; Stuart, J. A.; Marcy, D. L.; Hillebrecht, J.; Li, Q.; Ramos, L.; Jordan, K.; Fyvie, S.; et al. Characterization of the Branched-Photocycle Intermediates **P** and **Q** of Bacteriorhodopsin. *J. Phys. Chem. B* **2002**, *106*, 13352−13361.
(24) Maclaurin, D.; Venkatachalam, V.; Lee, H.; Cohen, A. E. Mechanism of voltage-sensitive fluorescence in a microbial rhodopsin. *Proc. Natl. Acad. Sci. U.S.A.* **2013**, *110*, 5939−5944.
(25) Touw, S. I.; de Groot, H. J.; Buda, F. Ab initio modeling of the spatial, electronic, and vibrational structure of Schiff base models for visual photoreceptors. *J. Phys. Chem. B* **2004**, *108*, 13560−13572.
(26) Rimai, L.; Heyde, M.; Gill, D. Vibrational spectra of some carotenoids and related linear polyenes. Raman spectroscopic study. *J. Am. Chem. Soc.* **1973**, *95*, 4493−4501.
(27) Doukas, A.; Aton, B.; Callender, R.; Ebrey, T. Resonance Raman studies of bovine metarhodopsin I and metarhodopsin II. *Biochemistry* **1978**, *17*, 2430−2435.
(28) Kochendoerfer, G. G.; Wang, Z.; Oprian, D. D.; Mathies, R. A. Resonance Raman examination of the wavelength regulation mechanism in human visual pigments. *Biochemistry* **1997**, *36*, 6577−6587.
(29) Hontani, Y.; Ganapathy, S.; Frehan, S.; Kloz, M.; De Grip, W. J.; Kennis, J. T. Strong pH-dependent near-infrared fluorescence in a microbial rhodopsin reconstituted with a red-shifting retinal analogue. *J. Phys. Chem. Lett.* **2018**, *9*, 6469−6474.
(30) Smith, S. O.; Pardoen, J. A.; Lugtenburg, J.; Mathies, R. A. Vibrational analysis of the 13-cis-retinal chromophore in dark-adapted bacteriorhodopsin. *J. Phys. Chem.* **1987**, *91*, 804−819.
(31) Smith, S. O.; Lugtenburg, J.; Mathies, R. A. Determination of retinal chromophore structure in bacteriorhodopsin with resonance Raman spectroscopy. *J. Am. Chem. Soc.* **1985**, *85*, 95−109.
(32) Hontani, Y.; Inoue, K.; Kloz, M.; Kato, Y.; Kandori, H.; Kennis, J. T. The photochemistry of sodium ion pump rhodopsin observed by watermarked femto-to submillisecond stimulated Raman spectroscopy. *Phys. Chem. Chem. Phys.* **2016**, *18*, 24729−24736.

https://doi.org/10.1021/acsphyschemau.3c00073
ACS Phys. Chem Au 2024, 4, 347−362

(33) Brown, L. S.; Dioumaev, A. K.; Lanyi, J. K.; Spudich, E. N.; Spudich, J. L. Photochemical Reaction Cycle and Proton Transfers in Neurospora Rhodopsin. *J. Biol. Chem.* **2001**, *276*, 32495−32505.
(34) Harris, A.; Ljumovic, M.; Bondar, A.-N.; Shibata, Y.; Ito, S.; Inoue, K.; Kandori, H.; Brown, L. S. A new group of eubacterial light-driven retinal-binding proton pumps with an unusual cytoplasmic proton donor. *Biochim. Biophys. Acta Bioenerg.* **2015**, *1847*, 1518−1529.
(35) Nakamizo, Y.; Fujisawa, T.; Kikukawa, T.; Okamura, A.; Baba, H.; Unno, M. Low-temperature Raman spectroscopy of sodium-pump rhodopsin from Indibacter alkaliphilus: Insight of Na+ binding for active Na+ transport. *Phys. Chem. Chem. Phys.* **2021**, *23*, 2072−2079.
(36) Iizuka, A.; Kajimoto, K.; Fujisawa, T.; Tsukamoto, T.; Aizawa, T.; Kamo, N.; Jung, K.-H.; Unno, M.; Demura, M.; Kikukawa, T. Functional importance of the oligomer formation of the cyanobacterial H+ pump Gloeobacter rhodopsin. *Sci. Rep.* **2019**, *9*, 10711.
(37) Waschuk, S. A.; Bezerra, A. G.; Shi, L.; Brown, L. S. Leptosphaeria rhodopsin: bacteriorhodopsin-like proton pump from a eukaryote. *Proc. Natl. Acad. Sci. U.S.A.* **2005**, *102*, 6879−6883.
(38) Dioumaev, A. K.; Wang, J. M.; Lanyi, J. K. Low-temperature FTIR study of multiple K intermediates in the photocycles of bacteriorhodopsin and xanthorhodopsin. *J. Phys. Chem. B* **2010**, *114*, 2920−2931.
(39) Smith, S. O.; Mathies, R. A. Resonance Raman spectra of the acidified and deionized forms of bacteriorhodopsin. *Biophys. J.* **1985**, *47*, 251−254.
(40) Asido, M.; Eberhardt, P.; Kriebel, C. N.; Braun, M.; Glaubitz, C.; Wachtveitl, J. Time-resolved IR spectroscopy reveals mechanistic details of ion transport in the sodium pump Krokinobacter eikastus rhodopsin 2. *Phys. Chem. Chem. Phys.* **2019**, *21*, 4461−4471.
(41) Ames, J. B.; Raap, J.; Lugtenburg, J.; Mathies, R. A. Resonance Raman study of halorhodopsin photocycle kinetics, chromophore structure, and chloride-pumping mechanism. *Biochemistry* **1992**, *31*, 12546−12554.
(42) Ohtani, H.; Itoh, H.; Shinmura, T. Time-resolved fluorometry of purple membrane of Halobacterium halobium O640 and an O-like red-shifted intermediate Q. *FEBS Lett.* **1992**, *305*, 6−8.
(43) Kojima, K.; Kurihara, R.; Sakamoto, M.; Takanashi, T.; Kuramochi, H.; Zhang, X. M.; Bito, H.; Tahara, T.; Sudo, Y. Comparative studies of the fluorescence properties of microbial rhodopsins: spontaneous emission versus photointermediate fluorescence. *J. Phys. Chem. B* **2020**, *124*, 7361−7367.
(44) Kouyama, T.; Kinosita, K.; Ikegami, A. Excited-state dynamics of bacteriorhodopsin. *Biophys. J.* **1985**, *47*, 43−54.
(45) Chang, C.-F.; Kuramochi, H.; Singh, M.; Abe-Yoshizumi, R.; Tsukuda, T.; Kandori, H.; Tahara, T. Acid−base equilibrium of the chromophore counterion results in distinct photoisomerization reactivity in the primary event of proteorhodopsin. *Phys. Chem. Chem. Phys.* **2019**, *21*, 25728−25734.
(46) Chang, C.-F.; Kuramochi, H.; Singh, M.; Abe-Yoshizumi, R.; Tsukuda, T.; Kandori, H.; Tahara, T. A unified view on varied ultrafast dynamics of the primary process in microbial rhodopsins. *Angew. Chem.* **2022**, *134*, No. e202111930.
(47) Nikolaev, D. M.; Shtyrov, A. A.; Vyazmin, S. Y.; Vasin, A. V.; Panov, M. S.; Ryazantsev, M. N. Fluorescence of the retinal chromophore in microbial and animal rhodopsins. *Int. J. Mol. Sci.* **2023**, *24*, 17269.
(48) Ernst, O. P.; Lodowski, D. T.; Elstner, M.; Hegemann, P.; Brown, L. S.; Kandori, H. Microbial and animal rhodopsins: structures, functions, and molecular mechanisms. *Chem. Rev.* **2014**, *114*, 126−163.
(49) Watanabe, H. C.; Ishikura, T.; Yamato, T. Theoretical modeling of the O-intermediate structure of bacteriorhodopsin. *Proteins* **2009**, *75*, 53−61.
(50) Maag, D.; Mast, T.; Elstner, M.; Cui, Q.; Kubař, T. O to bR transition in bacteriorhodopsin occurs through a proton hole mechanism. *Proc. Natl. Acad. Sci. U.S.A.* **2021**, *118*, No. e2024803118.
(51) Shtyrov, A. A.; Nikolaev, D. M.; Mironov, V. N.; Vasin, A. V.; Panov, M. S.; Tveryanovich, Y. S.; Ryazantsev, M. N. Simple models to study spectral properties of microbial and animal rhodopsins: evaluation of the electrostatic effect of charged and polar residues on the first absorption band maxima. *Int. J. Mol. Sci.* **2021**, *22*, 3029.
(52) Rath, P.; Krebs, M. P.; He, Y.; Khorana, H. G.; Rothschild, K. J. Fourier transform Raman spectroscopy of the bacteriorhodopsin mutant Tyr-185 .fwdarw. Phe: Formation of a stable O-like species during light adaptation and detection of its transient N-like photoproduct. *Biochemistry* **1993**, *32*, 2272−2281.
(53) Balashov, S. P.; Imasheva, E. S.; Govindjee, R.; Ebrey, T. G. Titration of aspartate-85 in bacteriorhodopsin: what it says about chromophore isomerization and proton release. *Biophys. J.* **1996**, *70*, 473−481.
(54) Richter, H.-T.; Brown, L. S.; Needleman, R.; Lanyi, J. K. A linkage of the pKa's of Asp-85 and Glu-204 forms part of the reprotonation switch of bacteriorhodopsin. *Biochemistry* **1996**, *35*, 4054−4062.
(55) Juarez, J. F. B.; Judge, P. J.; Adam, S.; Axford, D.; Vinals, J.; Birch, J.; Kwan, T. O.; Hoi, K. K.; Yen, H.-Y.; Vial, A. Structures of the archaerhodopsin-3 transporter reveal that disordering of internal water networks underpins receptor sensitization. *Nat. Commun.* **2021**, *12* (1), 1−10.
(56) Morgan, J. E.; Vakkasoglu, A. S.; Lanyi, J. K.; Lugtenburg, J.; Gennis, R. B.; Maeda, A. Structure changes upon deprotonation of the proton release group in the bacteriorhodopsin photocycle. *Biophys. J.* **2012**, *103*, 444−452.
(57) Rouhani, S.; Cartailler, J.-P.; Facciotti, M. T.; Walian, P.; Needleman, R.; Lanyi, J. K.; Glaeser, R. M.; Luecke, H. Crystal structure of the D85S mutant of bacteriorhodopsin: model of an O-like photocycle intermediate. *J. Mol. Biol.* **2001**, *313*, 615−628.
(58) Sonar, S.; Krebs, M. P.; Khorana, H. G.; Rothschild, K. J. Static and time-resolved absorption spectroscopy of the bacteriorhodopsin mutant Tyr-185 .fwdarw. Phe: Evidence for an equilibrium between bR570 and an O-like species. *Biochemistry* **1993**, *32*, 2263−2271.
(59) He, Y.; Krebs, M. P.; Fischer, W. B.; Khorana, H. G.; Rothschild, K. J. FTIR difference spectroscopy of the bacteriorhodopsin mutant Tyr-185 .fwdarw. Phe: Detection of a stable O-like species and characterization of its photocycle at low temperature. *Biochemistry* **1993**, *32*, 2282−2290.
(60) Hillebrecht, J. R.; Wise, K. J.; Koscielecki, J. F.; Birge, R. R. Directed evolution of bacteriorhodopsin for device applications. *Methods Enzymol.* **2004**, *388*, 333−347.
(61) Silapetere, A.; Hwang, S.; Hontani, Y.; Fernandez Lahore, R. G.; Balke, J.; Escobar, F. V.; Tros, M.; Konold, P. E.; Matis, R.; Croce, R.; et al. QuasAr Odyssey: the origin of fluorescence and its voltage sensitivity in microbial rhodopsins. *Nat. Commun.* **2022**, *13*, 5501.
(62) Fujimoto, K. J. Electronic Couplings and Electrostatic Interactions Behind the Light Absorption of Retinal Proteins. *Front. Mol. Biosci.* **2021**, *8*, 752700.
(63) Ryazantsev, M. N.; Altun, A.; Morokuma, K. Color tuning in rhodopsins: the origin of the spectral shift between the chloride-bound and anion-free forms of halorhodopsin. *J. Am. Chem. Soc.* **2012**, *134*, 5520−5523.
(64) Broser, M.; Spreen, A.; Konold, P. E.; Schiewer, E.; Adam, S.; Borin, V.; Schapiro, I.; Seifert, R.; Kennis, J. T.; Bernal Sierra, Y. A.; et al. NeoR, a near-infrared absorbing rhodopsin. *Nat. Commun.* **2020**, *11*, 5682.
(65) Palombo, R.; Barneschi, L.; Pedraza-González, L.; Padula, D.; Schapiro, I.; Olivucci, M. Retinal chromophore charge delocalization and confinement explain the extreme photophysics of Neorhodopsin. *Nat. Commun.* **2022**, *13*, 6652.
(66) Bruni, G. N.; Kralj, J. M. Membrane voltage dysregulation driven by metabolic dysfunction underlies bactericidal activity of aminoglycosides. *Elife* **2020**, *9*, No. e58706.
(67) Kralj, J. M.; Hochbaum, D. R.; Douglass, A. D.; Cohen, A. E. Electrical spiking in Escherichia coli probed with a fluorescent voltage-indicating protein. *Science* **2011**, *333*, 345−348.
(68) Zhang, J.; Yamazaki, Y.; Hikake, M.; Murakami, M.; Ihara, K.; Kouyama, T. Crystal structure of the O intermediate of the Leu93 - Ala mutant of bacteriorhodopsin. *Proteins* **2012**, *80*, 2384−2396.

https://doi.org/10.1021/acsphyschemau.3c00073
ACS Phys. Chem Au 2024, 4, 347−362

(69) Okumura, H.; Murakami, M.; Kouyama, T. Crystal structures of acid blue and alkaline purple forms of bacteriorhodopsin. *J. Mol. Biol.* **2005**, *351*, 481−495.
(70) Stamm, M.; Staritzbichler, R.; Khafizov, K.; Forrest, L. R. AlignMe—a membrane protein sequence alignment web server. *Nucleic Acids Res.* **2014**, *42*, W246−W251.
(71) Yang, J.; Yan, R.; Roy, A.; Xu, D.; Poisson, J.; Zhang, Y. The I-TASSER Suite: protein structure and function prediction. *Nat. Methods* **2015**, *12*, 7−8.
(72) Nikolaev, D. M.; Shtyrov, A. A.; Panov, M. S.; Jamal, A.; Chakchir, O. B.; Kochemirovsky, V. A.; Olivucci, M.; Ryazantsev, M. N. A comparative study of modern homology modeling algorithms for rhodopsin structure prediction. *ACS Omega* **2018**, *3*, 7555−7566.
(73) Morozenko, A.; Stuchebrukhov, A. Dowser++, a new method of hydrating protein structures. *Proteins* **2016**, *84*, 1347−1357.
(74) Olsson, M. H.; Søndergaard, C. R.; Rostkowski, M.; Jensen, J. H. PROPKA3: consistent treatment of internal and surface residues in empirical pKa predictions. *J. Chem. Theory Comput.* **2011**, *7*, 525−537.
(75) Dolinsky, T. J.; Czodrowski, P.; Li, H.; Nielsen, J. E.; Jensen, J. H.; Klebe, G.; Baker, N. A. PDB2PQR: expanding and upgrading automated preparation of biomolecular structures for molecular simulations. *Nucleic Acids Res.* **2007**, *35*, W522−W525.
(76) Nikolaev, D. M.; Manathunga, M.; Orozco-Gonzalez, Y.; Shtyrov, A. A.; Guerrero Martinez, Y. O.; Gozem, S.; Ryazantsev, M. N.; Coutinho, K.; Canuto, S.; Olivucci, M. Free Energy Computation for an Isomerizing Chromophore in a Molecular Cavity via the Average Solvent Electrostatic Configuration Model: Applications in Rhodopsin and Rhodopsin-Mimicking Systems. *J. Chem. Theory Comput.* **2021**, *17*, 5885−5895.
(77) Orozco-Gonzalez, Y.; Manathunga, M.; Marín, M. d. C.; Agathangelou, D.; Jung, K.-H.; Melaccio, F.; Ferré, N.; Haacke, S.; Coutinho, K.; Canuto, S.; et al. An Average Solvent Electrostatic Configuration Protocol for QM/MM Free Energy Optimization: Implementation and Application to Rhodopsin Systems. *J. Chem. Theory Comput.* **2017**, *13*, 6391−6404.
(78) Ryazantsev, M. N.; Nikolaev, D. M.; Struts, A. V.; Brown, M. F. Quantum mechanical and molecular mechanics modeling of membrane-embedded rhodopsins. *J. Membr. Biol.* **2019**, *252*, 425−449.
(79) Aquilante, F.; De Vico, L.; Ferré, N.; Ghigo, G.; Malmqvist, P.; Neogrády, P.; Pedersen, T. B.; Pitoňák, M.; Reiher, M.; Roos, B. O.; et al. MOLCAS 7: The Next Generation. *J. Comput. Chem.* **2010**, *31*, 224−247.
(80) Ponder, J. W.; et al. *TINKER: Software Tools for Molecular Design*; Washington University School of Medicine: Saint Louis, MO, 2004; Vol. 3.
(81) Neese, F. The ORCA program system. *Wiley Interdiscip. Rev.: Comput. Mol. Sci.* **2012**, *2* (1), 73−78.
(82) Frisch, M. J.; Trucks, G.; Schlegel, H.; Scuseria, G.; Robb, M.; Cheeseman, J.; Scalmani, G.; Barone, V.; Mennucci, B.; Petersson, G.; et al. *Gaussian 09*, Revision D. 01; Gaussian. Inc.: Wallingford, CT, 2009.
(83) Abraham, M. J.; Murtola, T.; Schulz, R.; Páll, S.; Smith, J. C.; Hess, B.; Lindahl, E. GROMACS: High performance molecular simulations through multi-level parallelism from laptops to supercomputers. *SoftwareX* **2015**, *1−2*, 19−25.
(84) Hornak, V.; Abel, R.; Okur, A.; Strockbine, B.; Roitberg, A.; Simmerling, C. Comparison of multiple Amber force fields and development of improved protein backbone parameters. *Proteins* **2006**, *65*, 712−725.
(85) Jambeck, J. P.; Lyubartsev, A. P. Derivation and systematic validation of a refined all-atom force field for phosphatidylcholine lipids. *J. Phys. Chem. B* **2012**, *116*, 3164−3179.
(86) Hayashi, S.; Tajkhorshid, E.; Schulten, K. Structural changes during the formation of early intermediates in the bacteriorhodopsin photocycle. *Biophys. J.* **2002**, *83*, 1281−1297.
(87) Darden, T.; York, D.; Pedersen, L. Particle mesh Ewald: An Nlog (N) method for Ewald sums in large systems. *J. Chem. Phys.* **1993**, *98*, 10089−10092.
(88) Evans, D. J.; Holian, B. L. The nose−hoover thermostat. *J. Chem. Phys.* **1985**, *83*, 4069−4074.
(89) Parrinello, M.; Rahman, A. Polymorphic transitions in single crystals: A new molecular dynamics method. *J. Appl. Phys.* **1981**, *52*, 7182−7190.
(90) Humphrey, W.; Dalke, A.; Schulten, K. VMD: visual molecular dynamics. *J. Mol. Graph.* **1996**, *14*, 33−38.

https://doi.org/10.1021/acsphyschemau.3c00073
ACS Phys. Chem Au 2024, 4, 347−362